

MEASUREMENTS OF CO REDSHIFTS WITH Z-SPEC FOR LENSED SUBMILLIMETER GALAXIES DISCOVERED IN THE H-ATLAS SURVEY

R. E. Lupu,^{1*} K. S. Scott,¹ J. E. Aguirre,¹ I. Aretxaga,² R. Auld,³ E. Barton,⁴ A. Beelen,⁵
F. Bertoldi,⁶ J. J. Bock,^{7,8} D. Bonfield,⁹ C. M. Bradford,^{7,8} S. Buttiglione,¹⁰ A. Cava,^{11,12}
D. L. Clements,¹³ J. Cooke,^{4,8} A. Cooray,⁴ H. Dannerbauer,¹⁴ A. Dariush,³ G. De Zotti,^{10,15}
L. Dunne,¹⁶ S. Dye,³ S. Eales,³ D. Frayer,¹⁷ J. Fritz,¹⁸ J. Glenn,¹⁹ D. H. Hughes,² E. Ibar,²⁰
R. J. Ivison,^{20,21} M. J. Jarvis,⁹ J. Kamenetzky,¹⁹ S. Kim,⁴ G. Lagache,^{22,23} L. Leeuw,^{24,25} S.
Maddox,¹⁶ P. R. Maloney,¹⁹ H. Matsuhara,²⁶ E. J. Murphy,²⁷ B. J. Naylor,⁷ M. Negrello,²⁸
H. Nguyen,⁷ A. Omont,²⁹ E. Pascale,³ M. Pohlen,³ E. Rigby,¹⁶ G. Rodighiero,³⁰ S.
Serjeant,²⁸ D. Smith,¹⁶ P. Temi,³¹ M. Thompson,⁹ I. Valtchanov,³² A. Verma,³³ J. D.
Vieira,⁸ J. Zmuidzinas^{7,8}

¹Department of Physics and Astronomy, University of Pennsylvania, Philadelphia, PA 19104, USA;
lroxana@sas.upenn.edu

²Instituto Nacional de Astrofísica, Óptica y Electrónica, Aptdo. Postal 51 y 216, 72000 Puebla, Mexico

³School of Physics and Astronomy, Cardiff University, The Parade, Cardiff, CF24 3AA, UK

⁴Department of Physics and Astronomy, University of California, Irvine, CA 92697, USA

⁵Institut d'Astrophysique spatiale bat 121 - Université Paris-Sud, 91405 Orsay Cedex, France

⁶Argelander Institute for Astronomy, Bonn University, Auf dem Huegel 71, 53121 Bonn, Germany

⁷Jet Propulsion Laboratory, Pasadena, CA 91109, USA

⁸California Institute of Technology, Pasadena, CA 91125, USA

⁹Centre for Astrophysics Research, Science and Technology Research Centre, University of Hertfordshire,
Herts AL10 9AB, UK

¹⁰INAF, Osservatorio Astronomico di Padova, Vicolo Osservatorio 5, I-35122 Padova, Italy

¹¹Instituto de Astrofísica de Canarias, C/Vía Láctea s/n, E-38200 La Laguna, Spain

¹²Departamento de Astrofísica, Universidad de La Laguna (ULL), E-38205 La Laguna, Tenerife, Spain

¹³Astrophysics Group, Physics Department, Blackett Lab, Imperial College London, Prince Consort Road,
London SW7 2AZ, UK

¹⁴Laboratoire AIM, CEA/DSM - CNRS - Université Paris Diderot, DAPNIA/Service d'Astrophysique,
CEA Saclay, Orme des Merisiers, F-91191 Gif-sur-Yvette Cedex, France

¹⁵Scuola Internazionale Superiore di Studi Avanzati, Via Bonomea 265, I-34136 Trieste, Italy

¹⁶School of Physics and Astronomy, University of Nottingham, University Park, Nottingham NG7 2RD, UK

¹⁷National Radio Astronomy Observatory, PO Box 2, Green Bank, WV 24944, USA

¹⁸Sterrenkundig Observatorium, Universiteit Gent, Krijgslaan 281 S9, B-9000 Gent, Belgium

¹⁹University of Colorado, CASA 389-UCB, Boulder, CO 80303, USA

²⁰UK Astronomy Technology Center, Royal Observatory Edinburgh, Edinburgh, EH9 3HJ, UK

²¹Scottish Universities Physics Alliance, Institute for Astronomy, University of Edinburgh, Royal
Observatory, Edinburgh, EH9 3HJ, UK

²²Université Paris-Sud 11, Institut d'Astrophysique Spatiale (IAS), UMR8617, F-91405 Orsay, France

²³CNRS, Orsay, F-91405, France

²⁴Physics Department, University of Johannesburg, PO Box 524, Auckland Park 2006, South Africa

²⁵SETI Institute, 515 N. Whisman Avenue Mountain View CA, 94043, USA

²⁶Institute for Space and Astronautical Science, Japan Aerospace and Exploration Agency, Sagami-hara, Japan

²⁷Infrared Processing and Analysis Center, Pasadena, CA 91125, USA

²⁸Department of Physics and Astronomy, The Open University, Walton Hall, Milton Keynes, MK7 6AA, UK

²⁹Institut d'Astrophysique de Paris, Université Pierre et Marie Curie and CNRS, 98 bis Boulevard Arago, 75014 Paris, France

³⁰Dipartimento di Astronomia, Università di Padova, Vicolo Osservatorio 2, I-35122 Padova, Italy

³¹Astrophysics Branch, NASA Ames Research Center, Mail Stop 245-6, Moffett Field, CA 94035, USA

³²Herschel Science Centre, European Space Astronomy Centre, European Space Agency, P.O. Box 78, 28691 Villanueva de la Cañada, Madrid, Spain

³³Oxford Astrophysics, Denys Wilkinson Building, University of Oxford, Keble Road, Oxford, OX1 3RH

ABSTRACT

A large fraction of the star formation activity in the Universe took place between $1 < z < 3$ in massive, dust-enshrouded galaxies. Understanding this submillimeter-bright galaxy population requires distance measurements from redshifts, but this has proved extremely challenging, both due to the large positional uncertainties of submillimeter instruments and heavy obscuration in the optical. Such problems can be circumvented by using multiple carbon monoxide (CO) lines observed simultaneously at millimeter wavelengths. We present new observations from Z-Spec, a broadband 200 - 300 GHz spectrometer, of sub-millimeter bright lensed sources recently detected by the Herschel Astrophysical Terahertz Large Area Survey (H-ATLAS). Four out of five sources observed were detected in CO, and their redshifts measured using a new redshift finding algorithm that uses combinations of the signal-to-noise of all the lines falling in the Z-Spec bandpass to determine redshifts with high confidence, even in cases where the signal-to-noise in individual lines is low. Lower limits for the dust masses (\sim a few $10^8 M_{\odot}$) and spatial extents (~ 1 kpc equivalent radius) are derived from the continuum spectral energy distributions, corresponding to dust temperatures between 54 and 69 K. The dust and gas properties, as determined by the CO line luminosities, are characteristic of dusty starburst galaxies, with star formation rates of $10^{2-3} M_{\odot} \text{ yr}^{-1}$. In the LTE approximation, we derive relatively low CO excitation temperatures ($\lesssim 100$ K) and optical depths ($\tau \lesssim 1$). Using a maximum likelihood technique, we perform a non-LTE excitation analysis of the detected CO lines in each galaxy to further constrain the bulk molecular gas properties. We find that the mid- J CO lines measured by Z-Spec localize the best solutions to either a high-temperature / low-density region, or a low-temperature

/ high-density region near the LTE solution, with the optical depth varying accordingly. Future observations of CO(1-0) or other molecular lines should help distinguish these scenarios and further illuminate the star-formation history of these galaxies.

Subject headings: submillimeter:galaxies — galaxies:distances and redshifts — galaxies:high-redshift — galaxies:starburst — carbon monoxide

1. INTRODUCTION

Galaxies detected by their thermal dust emission at submillimeter (submm) and millimeter (mm) wavelengths ($\lambda \approx 250 - 2000 \mu\text{m}$) comprise an important population of massive systems in the early Universe that are thought to be undergoing an early phase of intense star formation in their evolution (Blain et al. 2002). Dust grains within star-forming regions in these galaxies are heated by incident optical and ultraviolet (UV) radiation from young stars and thermally re-radiate this energy at far-infrared (far-IR) to mm wavelengths, with the peak of dust emission occurring at $\sim 60 - 200 \mu\text{m}$ in the rest-frame (Soifer & Neugebauer 1991). It is estimated that about half of all star-formation in the Universe is heavily obscured by dust and therefore difficult to identify in even the deepest surveys at optical/ultraviolet wavelengths (Puget et al. 1996). Observations at submm/mm wavelengths sample the Rayleigh-Jeans tail of the thermal dust spectrum, which rises steeply with frequency $\sim \nu^{3.5}$ (Dunne et al. 2000). For observations at $\lambda > 500 \mu\text{m}$, the climb up this steep spectrum with increasing redshift roughly cancels the effect of cosmological dimming with increasing distance (e.g., Blain et al. 2002), making galaxies with a fixed luminosity have roughly the same observed flux density at submm/mm wavelengths for redshifts between $1 < z < 10$. This allows a distance-independent study of dust-obscured star-formation and galaxy evolution spanning the epoch of peak star formation activity in the Universe ($z \sim 2 - 3$, e.g., Chapman et al. 2005).

Although first predicted by Low & Tucker (1968), the population of high-redshift and heavily dust-obscured galaxies (submillimeter galaxies, SMGs) was first revealed a decade ago (Smail et al. 1997), and several wide-area surveys at $850 \mu\text{m} - 1.2 \text{mm}$ have been carried out since then (e.g., Weiss et al. 2009b; Austermann et al. 2010; Coppin et al. 2006; Bertoldi et al. 2007; Scott et al. 2008), mapping a total of $\sim 4 \text{deg}^2$ of sky. More recently, much larger area surveys have been undertaken with the South Pole Telescope (SPT, Vieira et al. 2009) at $\lambda = 1.4 - 2 \text{mm}$, the Balloon-borne Large Aperture Submillimeter Telescope (BLAST, Pascale et al. 2008) at $\lambda = 250 - 500 \mu\text{m}$, and the *Herschel Space Observatory* (Pilbratt et al. 2010) at $\lambda = 55 - 670 \mu\text{m}$. Mapping a total area of $\sim 200 \text{deg}^2$ to

date (Pascale et al. 2008; Vieira et al. 2009; Eales et al. 2010), these surveys have uncovered a population of rare, and unusually bright, distant galaxies. Their inferred IR luminosities and high redshifts are consistent with a significant fraction of these extremely bright submm/mm galaxies being gravitationally lensed (Negrello et al. 2007), but proof requires extensive multi-wavelength follow-up campaigns. Their observed flux densities can be magnified by factors > 10 due to lensing by intervening foreground galaxies or clusters, as observed in similarly bright systems (e.g., Swinbank et al. 2010; Solomon & Vanden Bout 2005). By targeting lensed objects, we can study the typical properties of the star forming galaxies in the early Universe that would otherwise be inaccessible in a blank survey due to sensitivity limitations and source confusion. The ongoing Herschel-Astrophysical Terahertz Large Area Survey (H-ATLAS, Eales et al. 2010) in the Science Demonstration Phase (SDP) has already covered 14.4 deg^2 out of the $\sim 550 \text{ deg}^2$ planned, resulting in ~ 6600 sources (Clements et al. 2010; Rigby et al. 2010) with fluxes measured at 250, 350, and $500 \mu\text{m}$ using the Spectral and Photometric Imaging Receiver (SPIRE, Griffin et al. 2010; Pascale et al. 2010), and fluxes at 100 and $160 \mu\text{m}$ obtained with the Photodetector Array Camera and Spectrometer (PACS, Poglitsch et al. 2010; Ibar et al. 2010). Given the large areal coverage, H-ATLAS can detect the brightest (i.e. rarest) distant submm galaxies and is the first example where the efficient selection of lensed galaxies at submm wavelengths has been demonstrated (Negrello et al. 2010).

To understand the nature of these galaxies, in particular whether they represent a previously undiscovered population of intrinsically bright sources (e.g., Devriendt et al. 2010) or are relatively normal starburst galaxies lensed by foreground structures (e.g., Negrello et al. 2007), requires both complementary data at other wavelengths and measurements of their redshifts. However, measuring spectroscopic redshifts for these sources is challenging: their positional accuracy from submm/mm imaging is often poor due to diffraction limitations at these long wavelengths, and they tend to be highly extinguished by dust, making spectroscopic measurements from optical ground-based telescopes difficult (e.g., Chapman et al. 2005). Photometric redshifts obtained using submm bands are very useful for estimating the high redshift nature of such sources, but suffer from errors due to the degeneracy between the dust temperature and the redshift, which limit their precision to $\Delta z \approx 0.3$ (Aretxaga et al. 2007; Hughes et al. 2002). When the photometric redshift estimates involve SED template fitting, errors can also arise from our limited knowledge of the intrinsic SMG SED from FIR to radio, and its evolution with redshift. Combined with multi-wavelength data, training sets of spectroscopic redshifts may prove useful for reducing these errors for application to the large photometric datasets from ongoing and future surveys.

SMGs contain large reservoirs of molecular gas ($10^{10-11} M_{\odot}$, Tacconi et al. 2008), whose cooling is dominated by the rotational lines of CO, almost equally spaced by $\sim 115 \text{ GHz}$ in

the rest frame. Thus, the CO line detections at wavelengths between 1 cm and 1 mm (30-300 GHz) offer the most direct measurement of their redshifts. However, with the exception of only three other CO redshifts measured to date (Daddi et al. 2009; Weiss et al. 2009a; Swinbank et al. 2010), CO detections have largely been limited to SMGs whose redshifts were already known from optical spectroscopy (e.g., Frayer et al. 1998), as a consequence of the small instantaneous bandwidth of typical mm-wavelength receivers. Z-Spec overcomes this limitation due to its large bandwidth, covering the entire 1-1.5 mm atmospheric window, allowing simultaneous observations of multiple CO lines for galaxies at redshifts $z > 0.5$. Although the potential of using the CO ladder for redshift determination is well known (e.g., Silk & Spaans 1997), due to sensitivity limitations of current instruments, only large area submm surveys can provide a significant number of sources bright enough for such measurements.

These spectra can be used not only for an efficient redshift determination, but also to constrain the physical properties of the gas and dust (e.g., mass, density, temperature) in these galaxies (e.g., Bradford et al. 2009), by measuring the CO line strengths and the continuum slope. The analysis of the CO properties requires measurements of multiple CO lines, often involving the use of multiple instruments. To date, several spectral line energy distributions (SLEDs) for the CO molecule have been constructed for small mixed samples of galaxies and quasars (Papadopoulos et al. 2010; Wang et al. 2010; Bayet et al. 2009), or individual objects. Relatively well sampled CO SLEDs have been constructed from the ground for bright quasars (Weiß et al. 2007; Bradford et al. 2009; Danielson et al. 2010), while complete CO SLEDs have been measured by the *Herschel Space Observatory* in low redshift galaxies (Panuzzo et al. 2010; Van der Werf et al. 2010). Most SMGs have been observed in only one or two CO lines (see e.g., Harris et al. 2010; Ivison et al. 2010a; Aravena et al. 2010; Tacconi et al. 2008; Greve et al. 2005; Solomon & Vanden Bout 2005), and their physical properties remain largely unknown. This situation has improved in recent years, with observations of multiple CO lines in individual SMGs (Ao et al. 2008; Carilli et al. 2010; Lestrade et al. 2010; Riechers et al. 2010; Danielson et al. 2010). The best sampled CO SLEDs show that multiple CO components are required to explain the full line luminosity distribution, where most of the mid- J CO emission can generally be fit by a warm component, with kinetic temperatures of 40-60 K and gas volume densities of 10^3 - 10^4 cm^{-3} . However, solutions with kinetic temperatures of a few $\times 100$ K and lower densities are also allowed by the data (Ao et al. 2008; Weiß et al. 2007; Bayet et al. 2009), and this region of the parameter space has been insufficiently explored. Z-Spec has an important advantage over other instruments, since it covers a large portion of the CO SLED in a single observation (depending on the redshift) and with a common calibration for the entire bandpass.

This paper describes observations of five H-ATLAS sources undertaken with Z-Spec.

Based on the CO emission detected by Z-Spec, we successfully determined the redshifts of four out of five lensed galaxies. The Z-Spec observations are described in Section 2, followed by the description of the algorithm for redshift determination in Section 3. We use the measured redshift to constrain the spectral energy distribution (SED) of these galaxies, estimating the dust temperature and emissivity index, as well as the total infrared luminosity. We perform an analysis of the partial CO SLEDs, constructed from the lines observed by Z-Spec, to constrain the physical conditions of the molecular gas. The analysis of the galaxy SEDs and CO emission lines is presented in Section 4, and a summary of our results can be found in Section 5. Throughout the paper we assume a standard Λ CDM cosmology, with $H_0=71 \text{ km s}^{-1} \text{ Mpc}^{-1}$, $\Omega_M=0.27$, $\Omega_\Lambda=0.73$ (Spergel et al. 2007).

2. OBSERVATIONS AND DATA REDUCTION

We selected five high- z candidates among submm-bright galaxies with $F(500\mu\text{m}) > 100 \text{ mJy}$ (Table 1) from the H-ATLAS survey for follow-up observations with Z-Spec on the 10-m Caltech Submillimeter Observatory (CSO). Z-Spec is a single spatial pixel grating spectrometer with 160 silicon-nitride micro-mesh bolometer detectors (i.e. channels) operating from 190 – 308 GHz (Naylor et al. 2003; Earle et al. 2006; Bradford et al. 2009). The frequency response of the Z-Spec channels is approximately gaussian, with a variable FWHM from 720 to 1290 km s^{-1} over the bandpass, that is roughly equal to the channel separation (Earle et al. 2006). This follow-up was undertaken to confirm that these sources are lensed by lower redshift galaxy clusters or individual galaxies by measuring their redshifts directly at submm wavelengths. The redshifts of the foreground objects have been measured in the optical, and found to be much lower than the redshifts of the submm galaxies, consistent with the lensing scenario (Negrello et al. 2010). For convenience, throughout the paper we identify our targets by their names used in the SDP H-ATLAS catalogue (SDP.9, SDP.11, SDP.17, SDP.81, and SDP.130).

We carried out the Z-Spec observations of H-ATLAS sources at the CSO from 2010 March 07 - May 14 under generally good to excellent observing conditions, accumulating from 6.8 to 22.5 hour integrations on each target. The zenith opacity at 225 GHz (monitored by the CSO tau meter) was $\tau_{225\text{GHz}} = 0.06$ on average, and $\tau_{225\text{GHz}} \leq 0.07$ for 75% of the observations. A summary of the observations, including the total integration time on each source is given in Table 1.

The Z-Spec data were taken using the standard “chop-and-nod” mode in order to estimate and subtract the atmospheric signal from the raw data. The secondary mirror was chopped on- and off-source at a rate of 1.6 Hz with a chop throw of 90 arc-sec while stepping

through a 4-part nod cycle which position switches the primary mirror, integrating for 20 sec at each nod position. The chopping removes atmosphere fluctuations and the nodding removes instrumental offsets due to imperfect match between the two chopped positions. We checked the pointing every 2 – 4 hrs by observing quasars and other bright targets located close in elevation to the H-ATLAS targets, making small (typically < 10 arc-sec) adjustments to the telescope pointing model in real-time.

We analyze the data using customized software in the same manner as described in Bradford et al. (2009). For each channel, the nods are calibrated and averaged together, weighting by the inverse variance of the detector noise. Absolute calibration is determined by observations of Mars once per night, which we use to build a model of the flux conversion factor (from instrument Volts to Jy) as a function of each detector’s mean operating (“DC”) voltage (Bradford et al. 2009). Since the DC voltage depends on the combination of the bath temperature and the total optical loading on the detectors, we use these curves to determine appropriate calibration factors to apply to each nod individually. Based on the root mean square (rms) deviations of the Mars measurements from the best-fit curves, the channel calibration uncertainties are 3 – 8%, excluding the lowest frequencies for which a clean subtraction of the atmosphere is hindered by the pressure-broadened 183 GHz atmospheric water line. These uncertainties are propagated through the data reduction. The median rms uncertainties on the final co-added spectra for the H-ATLAS galaxies are listed in Table 1. These errors do not include the $\sim 5\%$ uncertainty on the brightness temperature of Mars (Wright 2007). The calibrated Z-Spec spectra of the five ATLAS galaxies are shown in Figures 1 and 2. The redshifts of these sources are determined using a custom algorithm, tailored specifically for multiple lines observed simultaneously in the same bandpass. This algorithm is presented in the next section.

3. REDSHIFT DETERMINATION

3.1. Algorithm Description

The redshift determination relies on the simultaneous detection of multiple CO and atomic lines. Using the multiple CO lines falling in the Z-Spec bandpass, we developed a redshift-finding algorithm that is capable of handling cases where the signal-to-noise in individual lines is low. The number of CO lines redshifted in the Z-Spec bandpass grows from 2 at $z = 0.51$ (CO(3-2) and CO(4-3)) to 4 or more at $z > 2$ (starting at CO(5-4) through CO(8-7)). The measurement of redshifts greater than ~ 3 requires the presence of high-excitation, warm CO gas, where transitions between higher rotational levels become important.

As the width of the Z-Spec channels varies from 720 to 1290 km s⁻¹ over the bandpass, larger than most observed line widths, most of the signal from one line will be concentrated in a single channel. The redshift finding algorithm uses two test statistics, E_1 and E_2 (Eqs. 1 and 2), constructed from combinations of the detection significance in those channels in which a reference line would be observed by Z-Spec at a given redshift z . The reference line list contains all CO rotational lines up to the CO(17-16) transition, the [C I] 492.16 GHz line, the [N II] 1458.8 GHz line, and the [C II] 1900.569 GHz line. For redshifts $z > 1$ the [C I] 809.342 GHz and CO(7-6) 806.651 GHz lines can fall in the same Z-Spec channel, and are therefore degenerate for the purpose of this procedure. The values of the test statistics are related to the probability that the lines from the reference list, redshifted by a factor of $(1 + z)$, are present in the spectrum. The null hypothesis is that there is no signal detected in the spectrum for any value of the redshift, and the distribution of the test statistics for the null hypothesis can be obtained using blank sky spectra, flat continuum sources, or noise simulations. Both statistics are maximized when the redshifted frequencies of the reference lines match the frequencies where the largest signal is present in the spectra, after continuum subtraction. The continuum subtraction uses a fourth degree polynomial to better account for local deviations from a power-law. The use of two statistics instead of one helps reduce the number of false redshifts that can be due to random noise fluctuation in the spectra.

We search a redshift range between 0.6 and 5.6 in steps of 0.001. Let $n(z)$ be the number of reference lines that would fall in the Z-Spec bandpass at redshift z . The algorithm loops through all the z values, redshifting all the lines in the line list, and finding the set of $n(z)$ Z-Spec channels corresponding to the lines in the bandpass at that redshift. The two test statistics, E_1 and E_2 , are evaluated for each redshift using the signal and noise in the set of $n(z)$ channels determined in the previous step. The first test statistic, $E_1(z)$, is defined as the ratio of the signal to the noise summed only over the Z-Spec channels that correspond to a line in our list when redshifted to redshift z ,

$$E_1(z) = \frac{\sum_i S_i}{\sqrt{\sum_i \sigma_i^2}}, \quad (1)$$

where the sum is taken from 1 to $n(z)$, and S_i and σ_i are the continuum subtracted signal and noise, respectively, for the channel corresponding to line i . The second test statistic, $E_2(z)$, is defined as

$$E_2(z) = \text{median}\{f_{ij} | f_{ij} = 0.5(S_i/\sigma_i + S_j/\sigma_j), 1 \leq i, j \leq n(z), i < j\}, \quad (2)$$

where the set contains all possible pairs of lines in the Z-Spec bandpass at the corresponding

redshift. The E_2 statistic can be easily understood as a rejection criterion. Setting $E_2 = \epsilon$ as a lower limit is equivalent to discarding all redshifts for which the median value of the average S/N in any pair of channels is less than ϵ . Note that E_1 would be a reasonable statistic for single line detections, but E_2 relies on multiple lines being present in the Z-Spec bandpass at a given redshift. For redshifts < 0.6 , E_1 is still a useful statistic, though the presence of only one line does not make for an unambiguous redshift determination.

No a priori knowledge of the relative line strengths is assumed, and therefore the algorithm gives equal weight to all the lines in the search list. As such, the significance of the determined redshift is dependent on which lines are detected in the spectrum relative to the lines that were expected based on the reference list. This is the case for SDP.17b (see Section 3.3), where the redshift significance increases greatly if we include the water line on our line list. However, such an extension of the reference line list is not always justified, since the significance for the redshift of another galaxy where the water line is not detected would be unnecessarily diminished. Care must also be taken in using the current line list at higher redshifts, where the high J CO lines are likely to have much lower significance relative to the [N II] and [C II] lines. For example, the strength of the CO lines drops with increasing J for starburst galaxies (e.g., Danielson et al. 2010), but remains relatively constant for AGN-dominated galaxies and quasars (e.g., Bradford et al. 2009; Van der Werf et al. 2010). Current knowledge of line strengths and the nature of the sources at high redshift does not warrant including this information in the redshift search.

3.2. Testing the Method: Simulations on Blank Sky

The distributions of E_1 and E_2 , as well as the effect of noise on the positions of their maxima, have been confirmed by simulating multiple realizations of *blank sky* spectra. The simulations take an input spectrum and generate new realizations by choosing random values of the signal in each channel, normally distributed around the value of the input signal in that channel, with a standard deviation equal to the measurement error in the same channel. The error array associated with the new realization is scaled accordingly, such that the signal-to-noise in each channel is equal to that of the input spectrum. As the input spectrum we used a 6.5 hour integration on blank sky, recorded on May 11 and 12, 2010. Other featureless spectra can also be used for this test. For each realization, we calculate the values of both test statistics and determine the redshifts corresponding to their maxima. The distribution of these redshifts is shown in Figure 3, derived from a simulation containing 1000 realizations of the sky spectrum. Ideally, this distribution should be uniform, but the input sky spectrum is not perfectly smooth, possibly due to small instrumental artefacts, which are reflected by the

probability variations. The noise cross-correlation between channels are present in the initial sky spectrum, but not in the simulated spectra. We find that although the *values* of E_1 and E_2 for each redshift are mostly correlated, the *locations of their maxima* are not (Pearson correlation coefficient 0.15). Figure 3 conveys this fact by comparing the maximum joint probability that E_1 and E_2 select the same redshift, relative to the maximum probability of a redshift found by E_1 independently ($\sim 3\%$ vs. $\sim 17\%$). This shows that the combination of two test statistics is more robust against random fluctuations, considerably reducing the noise floor across the redshift range.

A realization of the two test statistics using a blank sky spectrum is shown in Figure 4. In this case, the maxima of the two statistics occur for different redshifts, and no value of E_2 is above the threshold of 2. For noise-dominated spectra, such as blank sky, $E_1(z)$ is well fit by a normal distribution with $\sigma_{E_1}=0.97$, and $E_2(z)$ by a t distribution with 10 degrees of freedom (Figure 5). For our redshift determination, we first ask that the maximum value of E_1 have a significance $\geq 3\sigma$. Equivalently, the null is rejected at 99.73% confidence level. However, as noise fluctuations can still lead to random, albeit significant, peaks in these statistics even for blank sky spectra, the redshift confirmation also requires that the maxima of the two test statistics occur at the same redshift. To summarize, a redshift z_0 is accepted when the following conditions hold:

$$\begin{aligned} E_1(z_0) &\geq 3\sigma_{E_1}, \\ E_1(z_0) &= \max(E_1), \\ E_2(z_0) &= \max(E_2). \end{aligned} \tag{3}$$

For a line pair, the E_1 3σ threshold corresponds to an average S/N per channel of 2.12. Z-Spec reaches a sensitivity of about $0.5 \text{ Jy s}^{1/2}$ per channel for an atmospheric optical depth $\tau_{225}=0.068$ (Inami et al. 2008). Combining the 3σ threshold criterion with the measured sensitivity of Z-Spec, we estimate that a redshift can be determined in less than 1.5 hours of integration time if the line flux densities per channel are on the order of 15 mJy, but can require more than 12.5 hours if the flux density is less than 5 mJy. For our galaxy sample, the mean integrated CO line flux (Table 3) is $\sim 18 \text{ Jy km s}^{-1}$, while the average width of the channels is 950 km s^{-1} . However, the flux density per channel could be only $\sim 10 \text{ mJy}$ if the line flux happens to be split between two adjacent channels. In this case, the typical integration time for obtaining a redshift with Z-Spec would be at least 3.5 hours.

3.3. Comments on Individual Redshifts

The results of applying this algorithm to our galaxy sample are shown in Figure 6. The redshift value and its uncertainty (Table 2) are determined from the position and width of the peak of the E_1 test statistic, and the significance of the redshift peak is tested against the null hypothesis (Figure 7). We fit a gaussian to the peak of the $E_1(z)$ statistic, and define the redshift error as the upper limit for the standard deviation of this gaussian. When lines are present in the spectrum, aside from the main peak due to the true redshift, secondary peaks will arise in the E_1 and E_2 distributions, corresponding to redshifts where some of the lines in the line list fall on the same channels as the observed lines. The secondary peaks are marked by blue asterisks for each source in Figure 6. The real redshift will have higher significance than these secondary peaks, since the largest number of lines add their contribution to the total signal in this case. Excluding the true redshift and all the redshifts corresponding to secondary peaks from the test statistics, we are left with the null distribution, as shown in Figure 7. This figure also shows the significance of the redshift determination for each source, by marking the position of the peak value of the test statistic relative to the 3σ threshold.

SDP.81 The redshift for SDP.81, $z=3.037\pm 0.01$, obtained by this method at 3.8σ significance on 19 March 2010, was confirmed ($z=3.042\pm 0.001$) with follow-up observations with the IRAM Plateau de Bure Interferometer on 23 March 2010 (IRAM/PdBI, Negrello et al. 2010; Neri et al. 2010) and with an independent blind search on 25 March 2010 by the Zpectrometer instrument at the Green Bank Telescope (GBT/Zpectrometer, Negrello et al. 2010; Frayer et al. 2010), informed by a concurrent photometric redshift estimate ($2.9_{-0.3}^{+0.2}$). The significance of the test statistics for our redshift determinations shows that the integration time necessary to secure a redshift can be much shorter than the values listed in Table 1, and future submm instruments with better sensitivity will be able to obtain the redshifts of such galaxies even faster.

SDP.17 Given the size of the Z-Spec beam ($\text{FWHM}\approx 30''$) and the possible presence of lensing or other foreground structures in the same beam, the observed spectrum could be a combination of features from multiple objects. We choose this interpretation for the spectrum of SDP.17, best described by two components at different redshifts (both listed in Table 2). The first redshift found by our algorithm is 2.308 (SDP.17b). After fitting the CO lines at this redshift and subtracting them from the spectrum, we perform a second redshift determination, identifying a second component with a redshift of 0.942 (SDP.17a). This combination explains all the features present in the spectrum (see Figure 2), and is consistent with the interpretation of the 299 GHz feature as the restframe 987 GHz water line at a redshift of 2.308. This water line has been seen to be very strong in other AGN and star-forming galaxies at low redshift, such as Mrk231 and Arp 220 (González-Alfonso et al. 2010),

and it has been tentatively detected in the Cloverleaf quasar at $z=2.56$ by Bradford et al. (2009). The redshifts of SDP.9 and SDP.17b have recently been confirmed by follow-up observations of the CO(2-1) and (3-2) lines, respectively (L. Leeuw, private communication), with the Combined Array for Research in Millimeter-wave Astronomy (CARMA). The second redshift (SDP.17a) has a much lower significance, but it is in agreement with the photometric and spectroscopic optical redshifts (0.77 ± 0.13 and 0.9435 ± 0.0009 , respectively Negrello et al. 2010). Alternatively, the peak now identified with the CO(5-4) line at $z=0.94$ could be a wing of this water line, due to a ~ 1600 km s $^{-1}$ outflow. The presence of multiple ULIRGs in a single line of sight is intriguing, and is an example of discoveries that can be made possible by Z-Spec’s broad bandwidth.

SDP.130 SDP.130 has a redshift of 2.6260 ± 0.0003 , measured by GBT/Zpectrometer ($z=6.625\pm 0.001$, Frayer et al. 2010), and made more precise with PdBI/IRAM (Negrello et al. 2010; Neri et al. 2010). So far, three CO lines have been measured in this galaxy at this redshift, namely the CO(1-0) line observed with the Zpectrometer, and the CO(3-2) and CO(5-4) lines observed with PdBI (Negrello et al. 2010), on a tuning that was successfully guided by the sub-mm photometric redshift of $z = 2.6_{-0.2}^{+0.4}$ (Negrello et al. 2010). However, we do not detect any of the higher J transitions ($J_u > 6$) that would fall in the Z-Spec bandpass at this redshift. This non-detection, which places upper limits on the integrated fluxes of the CO (6-5) through (9-8) lines at < 12.5 Jy km s $^{-1}$, suggests a low (< 50 K) gas temperature in the $z=2.626$ galaxy. We attempted to identify the line at 277 GHz, marked in red in Figure 1, with the CO (3-2) transition at $z=0.25$, but that would be inconsistent with the optical spectroscopic redshift of the lensing galaxy (0.220 ± 0.002 , Negrello et al. 2010) by more than 7000 km s $^{-1}$, as well as inconsistent with the other observed properties of the foreground galaxy. Similarly, identifying this feature with the 987 GHz water line at $z=2.626$ would require a velocity offset of ~ 4200 km s $^{-1}$, and usually the presence of highly excited CO gas, which is not observed. This feature remains unidentified.

SDP.9 and SDP.11 The redshifts for these galaxies have been measured at 6.5σ and 5.3σ significance, respectively. The redshift of SDP.9 has been confirmed by CARMA observations, and more follow-up observations are currently planned for both SDP.9 and SDP.11.

4. GAS AND DUST PROPERTIES

A model including the lines and power-law continuum is fit to each spectrum in Figures 1 and 2, allowing the line intensities, redshift, and continuum slope to vary. The best fit power-law index α for each galaxy is listed in Table 2. The initial estimate for the redshift is provided by the algorithm described above, and the fit is constrained by the requirement that

all the lines be at the same redshift. In cases where some of the lines are blended, we first fit only the unblended lines to obtain a more precise value for the redshift, and then we fit all the lines simultaneously, with the redshift kept fixed, to get the integrated line strengths, listed in Table 3. Although the lines are not resolved, the signal from one line can be spread among adjacent channels due to the overlap of their frequency responses. We measure only the integrated line strengths, taking into account the frequency response of each Z-Spec channel, weighted according to the line width. On average, line widths below $\sim 1000 \text{ km s}^{-1}$ are not resolved by Z-Spec, and we choose a value of 300 km s^{-1} in fitting the integrated line strengths. This value closely matches the width of the lines for SDP.81 and SDP.130 at PdBI (Neri et al. 2010), but is relatively low compared to the range found by interferometric measurements of other lensed high-redshift galaxies (Greve et al. 2005; Knudsen et al. 2009). However, the determination of the integrated line fluxes is not sensitive to the choice of the line width up to values of the order of the channel width. The largest uncertainties in the integrated line strengths arise in the case of line blending, such as the CO(7-6) and [C I] $^3P_2 \rightarrow ^3P_1$ lines, or the overlapping lines at different redshifts in SDP.17 (blended lines are indicated in Table 3).

4.1. Continuum Spectral Energy Distributions

The continuum data for all 5 galaxies is shown in Figure 8. The measured continuum flux from Z-Spec is found to be in good agreement with the MAMBO 1.2 mm photometry (Negrello et al. 2010), except for SDP.9. Estimates of the total amount of dust and star formation rates in each galaxy can be obtained by fitting their far-infrared (far-IR) to submillimeter spectral energy distribution (SED). In this fit we include the Z-Spec data along with the Herschel-SPIRE and Herschel-PACS photometric points, as well as the Submillimeter Array (SMA) measurements at $880 \mu\text{m}$ for SDP.81 and SDP.130 (Negrello et al. 2010).

The far-IR rest frame SED can be described by a modified blackbody function, defined as

$$F_\nu = Q_\nu(\beta)B_\nu(T_d)\Omega_d = (1 - e^{-\tau(\nu_0)(\nu/\nu_0)^\beta}) \frac{2h\nu^3}{c^2} \frac{1}{e^{h\nu/kT_d} - 1} \Omega_d = \frac{L_{IR}}{4\pi d^2} \frac{Q_\nu(\beta)B_\nu(T_d)}{\int Q_\nu(\beta)B_\nu(T_d)d\nu}, \quad (4)$$

where $B_\nu(T_d)$ is the Planck function, $\tau(\nu_0) = 1$ is the optical depth at ν_0 , Ω_d represents the observed solid angle of the dust emitting region, d is the (known) distance to the source, and h and k denote the Planck and Boltzmann constant, respectively. The fit can be performed with three parameters: T_d , β , and a scale factor. The overall scale of the SED can be

parametrized either in terms of the solid angle Ω_d , or the total infrared luminosity (L_{IR}), defined as the integral of the SED from 8 to 1000 μm (rest frame). The L_{IR} derived in this manner underestimates the true total infrared luminosity, due to the likely presence of warmer dust components that contribute at shorter wavelengths. Including ν_0 as a fourth parameter in the fit leads to a value of 1251 ± 130 GHz for SDP.9, but no strong constraints are found for the rest of the sample. The low value found for ν_0 , and the observed flattening of the peak of the SEDs in the far-IR suggest that the SEDs of the galaxies in our sample can be modeled either as combinations of multiple graybodies with different temperatures, or as a single graybody with a large optical depth at far-IR wavelengths.

The simplest model that can reproduce the data for the entire sample has fixed $\beta = 2$ (Priddey & McMahon 2001) and $\nu_0 = 1300$ GHz, in agreement to the value found for SDP.9. The dust emissivity index $\beta = 2$ is also consistent with the error bars of the Z-Spec spectra. The best-fit models are shown in Figure 8, and the corresponding values for T_d are listed in Table 2. With dust temperatures between 54 and 69 K, the peak of the dust SED is found in a narrow range of wavelengths (73 to 92 μm) for all lensed galaxies in the sample. It is important to bear in mind that this fitting function for the SED is largely empirical, and the degree to which T_d and β represent physical quantities is complicated by the spatial averaging over the entire galaxy and the degeneracy between a distribution in dust temperature and a distribution of dust types (represented by β). The formal errors for the fitted parameters (T_d) should not be interpreted as errors on physical quantities, due to these caveats.

Even though such SED fits could be obtained using just the photometric points, the addition of Z-Spec data not only strongly constrains the continuum slope, but also breaks the degeneracy between T_d and redshift (Blain 1999), by independently determining the latter. Since Z-Spec has determined the redshift, we are able to obtain T_d from the continuum fit, which otherwise would constrain the quantity $T_d/(1+z)$ (e.g., Amblard et al. 2010). This degeneracy can lead to significant variations in the derived T_d if the redshift is not measured independently. The implications of the continuum slope measured by Z-Spec for the dust composition will be analyzed in a future work.

Using Eq. 4 corrected for redshift and the derived T_d , we can estimate the observed size of the dust emitting region. This solid angle will be affected by the lensing magnification factor. If the dust optical depth at submm wavelengths is low, as is often the case, Ω_d will be correlated with τ , and therefore with β (Hughes et al. 1993). However, we break this degeneracy by fixing β . The resulting Ω_d ranges between 0.30 arcsec² for SDP.17b and 1.44 arcsec² for SDP.17a. These values may underestimate source sizes that are resolved in the SMA images with a resolution of ~ 0.8 arcsec at 340 GHz. Using the magnification factors from Table 2, the intrinsic size of the dust emitting region will have an equivalent radius

of 0.7 kpc for SDP.81 and 1.3 kpc for SDP.130. Note however, that Ω_d corresponds to the effective solid angle of the dust emitting region, such as the total area of small clumps spread over a larger region. In an image where these clumps are unresolved, the total observed solid angle can appear to be larger.

Having estimated the source size, the total dust mass follows from the relationship $\tau(\nu) = \kappa(\nu)M_d/D_A^2\Omega_d$, with $\kappa(\nu) = 0.4(\nu/250\text{GHz})^\beta$ (e.g., Weiß et al. 2007), where D_A is the angular diameter distance. The dust mass can also be estimated in the optically thin limit ($1 - e^{-\tau} \simeq \tau$) without the additional step of deriving Ω_d , by substituting $\tau(\nu)$ directly in Equation 4. This is a good approximation at 250 GHz (1.2 mm), in the middle of the Z-Spec bandpass. Calculated in the optically thin limit, the dust mass is a robust estimate of the lower limit for the total dust mass in the galaxy, $M_{d,lim}$. Using the optically thin approximation and the 250 GHz flux density measured by Z-Spec, we derive values for the magnified $M_{d,lim}$ of a few $\times 10^9 M_\odot$, as listed in Table 2. As the value of $\kappa(\nu)$ at 250 GHz is not dependent on β , the derived dust mass will be affected only by the optical depth and T_d . If the dust is optically thick, as suggested by $\nu_0=1300$ GHz, the calculated $M_{d,lim}$ will underestimate the true dust mass for our galaxy sample by at most 30%. The dust mass is also inversely correlated with the assumed temperature, and will be underestimated when using the dust temperature corresponding to the peak of the SED. This temperature is likely too large to represent the bulk of the dust. Assuming that the 250 GHz flux is partially due to a dust component with a temperature as low as 20 K, and taking into account the optical depth corrections, we estimate that the total dust mass could be larger than $M_{d,lim}$ by up to a factor of ~ 4 . To summarize, with good approximation, the true dust masses for these galaxies will be found in the interval $[1, 4] \times M_{d,lim}$. The uncertainties in $M_{d,lim}$ are mostly due to uncertainties in the expression for $\kappa(\nu)$. Note that the quantity M_d/Ω_d is proportional to τ and independent of temperature; for a given τ , a lower limit for M_d implies a lower limit for Ω_d , but this limit for Ω_d will decrease with increasing τ .

A more realistic approach is to fit the photometric and continuum points with a library of SEDs, taking into account the transmission curve of each instrument. We apply this method to our galaxy sample, using the SED libraries of Chary & Elbaz (2001) (CE01), and Dale & Helou (2002) (DH02). We find that the IR luminosities derived from the modified blackbody fitting are at most factor of ~ 2 lower than those when we use the SED libraries, and within 20% from the L_{IR} obtained assuming the models of da Cunha et al. (2008), calibrated for ULIRGs, with $A_V > 2$ (Negrello et al. 2010). The variations between the values of L_{IR} obtained by different methods reflect the systematic uncertainties in deriving this quantity. Similar underestimates have been found by others, and are due to the fact that the submm photometry does not measure the warm dust component of the SED, if one is present (Swinbank et al. 2010; Ivison et al. 2010b). This is emphasized by the poor fit of

the modified blackbody curve to the Herschel-PACS data points, and the significant flux at shorter wavelengths predicted by the CE01 and DH02 models (Figure 8). Any derivation of L_{IR} is model dependent, with the largest differences arising from the presence of a warm dust component in the SED libraries. In Table 2 we list the L_{IR} values derived from the SED template fitting method, as they represent a more accurate description of the total infrared energy output than the modified blackbody. On average, our L_{IR} values are about 25% lower than those found by Negrello et al. (2010), but these differences are difficult to judge without data shortward of $100 \mu\text{m}$. Note that these values are rather smaller than typical IR luminosities of classical SMGs and unbiased sources detected by Herschel surveys.

Except for SDP.17, we attribute all the submm flux density to the high redshift galaxy. The foreground lenses for the other galaxies in our sample have optical properties consistent with being quiescent elliptical galaxies, and are therefore unlikely to have a significant submm emission. We have attempted a decomposition of the SDP.17 SED, using the two measured redshifts and a wavelength-independent scaling factor for each of the two components. The χ^2 value for the SED template fits is minimized when the observed flux density is split in half between the two components. This factor has been taken into account in Figure 8 and in deriving the L_{IR} for SDP.17a and SDP.17b, as listed in Table 2. However, the large dust mass inferred for SDP.17a could be an indication that the SED decomposition between SDP.17a and SDP.17b overestimates the contribution of SDP.17a.

We estimate the star formation rates for our galaxy sample using the conversion factor $SFR(M_{\odot} \text{ yr}^{-1}) = 1.5 \times 10^{-10} (L_{IR}/L_{\odot})$ (Solomon et al. 1997). Since the selected galaxies are lensed by foreground objects with magnification factors ~ 10 (Negrello et al. 2010), the intrinsic IR and CO line luminosities will be ~ 10 times lower than the direct conversion from the measured fluxes. SDP.81 and SDP.130 have magnification factors of 25 and 6, respectively, as derived from the best-fit lens model to the high-resolution sub-mm images available for these two objects (Negrello et al. 2010). In Tables 2 and 4, we left the quantities affected by gravitational lensing magnification unmodified, for reference, but the presence of this contribution is indicated by the letter μ in front. Based on model predictions (Negrello et al. 2007), a typical amplification factor of 10 can be applied to these values. Once corrected for magnification, the infrared luminosities and corresponding SFRs are those typical of Ultra Luminous Infrared Galaxies (ULIRGs).

4.2. CO Line Luminosities and Spectral Energy Distributions

The measurements of CO lines reveal important information about the physical properties and excitation conditions of the molecular gas, as well as the total gas budget in these

galaxies. These parameters can be used to investigate the link between star formation and gas properties. Higher gas temperatures and lower densities would suggest that the star formation has been quenched, while lower temperatures associated with higher densities would show that most of the gas in the galaxy is still collapsing and forming stars. This follows from the fact that the Jeans mass increases rapidly at higher temperatures and low densities.

A useful quantity describing the CO lines is the velocity-integrated brightness temperature scaled by the area of the source, L'_{CO} , in units of $\text{K km s}^{-1} \text{pc}^2$. In what follows, the brightness temperatures are computed in the Rayleigh-Jeans limit. If the CO is thermalized and the lines are optically thick, L'_{CO} will be the same for all rotational transitions for which the Rayleigh-Jeans approximation holds. This quantity is traditionally derived from the CO(1-0) transition and related to the total molecular mass via the empirical relation $M_{gas} = \alpha L'_{CO}$, where α is $4.6 M_{\odot} (\text{K km s}^{-1} \text{pc}^2)^{-1}$ for the Galaxy (Solomon et al. 1997), and $0.8 M_{\odot} (\text{K km s}^{-1} \text{pc}^2)^{-1}$ for ULIRGs (Solomon & Vanden Bout 2005; Tacconi et al. 2008). Following Solomon & Vanden Bout (2005), we can use the latter value for α and the L'_{CO} for the lowest observed CO transition to determine the gas masses. This procedure assumes that all transitions from CO(1-0) up to the lowest observed are thermalized, which might not necessarily be the case. A recent comparison of the CO(3-2) and (1-0) lines (Harris et al. 2010) shows that the ratio of the brightness temperatures for these two lines averages to 0.6 rather than 1, due to the presence of multi-phase CO gas. Moreover, the mid- J CO transitions do not account for the possible presence of a colder gas component, making the M_{gas} derived in this manner a lower limit for the total gas mass in the galaxy. Assuming that the lines with $J_u > 3$ are thermalized, corresponding to a warmer gas component, we apply this correction factor to the lowest CO transition measured, and obtain the gas masses listed in Table 4. These values result in an average molecular gas-to-dust ratio for the lensed galaxies of 34 ± 10 , independent of magnification. The mean does not include the foreground SDP.17a, and is in agreement with the values found for other SMG samples (Kovács et al. 2006; Michałowski et al. 2010; Santini et al. 2010).

Using the SFRs derived from the IR luminosities, the gas reservoir probed by CO implies a gas depletion time $[M_{gas}/L_{IR}]$ in these objects of $\sim 10^7$ years, similar to other known SMGs (Solomon & Vanden Bout 2005; Greve et al. 2005). This can be interpreted as the starburst lifetime under the assumptions of constant SFR and no gas inflow. Note that this estimate of the gas depletion time is independent of lensing magnification. The star formation efficiency can be expressed directly in terms of L_{IR}/L'_{CO} , without the need for a gas mass conversion factor. After accounting for the lensing magnification factor, L_{IR} and L'_{CO} for our sample follow the same relationship as other SMGs and ULIRGs (Greve et al. 2005; Wang et al. 2010), within the scatter.

In order to derive the physical characteristics of the gas in these galaxies, including the gas temperature, density, pressure, and CO column density, we need measurements of multiple CO transitions, sampling the rotational ladder as well as possible. The spectral line energy distribution (SLED) for the CO molecule has been constructed in a few cases for nearby and low redshift galaxies (e.g., Panuzzo et al. 2010). In Figure 9 we show the partial SLEDs for our galaxy sample, constructed from the lines detected in the Z-Spec bandpass. This plot favors a distribution with the brightest lines between CO(5-4) and (7-6), similar to the distribution observed for other SMGs and starburst galaxies (Weiss et al. 2007; Danielson et al. 2010). The shape of the line luminosity distribution does not reflect only the CO excitation temperature, but also the gas density, and the effects of the optical depth at the line frequency (Goldsmith & Langer 1999; Papadopoulos et al. 2010). In the optically thin limit, the CO column density scales with the absolute value of the line intensity, assuming that the source size and the magnification factor are known. Under the assumption of local thermodynamic equilibrium (LTE), all CO transitions have the same excitation temperature, T_{ex} , also equal to the gas kinetic temperature T_{kin} , signifying that all rotational levels are populated according to the Maxwell-Boltzmann distribution at temperature T_{ex} . In Section 4.2.1 we estimate these parameters by fitting the partial SLEDs, using the relationship between the integrated line brightness temperature, column density and excitation temperature, under LTE. Although this case is limiting due to the assumption of constant T_{ex} for all levels, it is interesting to compare the predictions of this model to the more general non-LTE models, given its simple physical interpretation. In the non-LTE case, presented in Section 4.2.2, the models involve a larger number of parameters, and are less well constrained. We use RADEX (van der Tak et al. 2007) to compute the brightness temperatures of the CO lines and estimate the likelihood distribution over the parameter space. These distributions allow us to assess if the available data are able to distinguish between the LTE and non-LTE models.

4.2.1. LTE models

The integrated line flux $S_\nu \Delta v$ (in Jy km s⁻¹) in the observer's frame is related to the velocity-integrated Rayleigh-Jeans source brightness $W(J)$ by (e.g., Solomon et al. 1997)

$$W(J) = \frac{\lambda_{J,J-1,rest}^2 (1+z)^3}{2k\Omega_a} S_\nu \Delta v \frac{\Omega_a}{\Omega_s} \quad (5)$$

where Ω_s and Ω_a are the solid angles of the source and the antenna, respectively. $W(J)$ is in units of K km s⁻¹. The last fraction represents the inverse of the beam filling fraction. The

contribution of the gravitational lensing magnification should cancel out in this expression, as it contributes to both S_ν and Ω_s , but the true Ω_s is not known. In principle, the same approach taken for the continuum (Section 4.1) could be used to determine the source size. However, such a fit requires a minimum of three parameters, and will not be well constrained by the number of CO lines in our SLEDs. In addition, the optical depth depends directly on the column density, and cannot be estimated independently, in the same way that the dust optical depth was determined by the continuum slope. We assume an intrinsic source size of ~ 2 kpc, consistent with the angular diameter of $0.2''$ found for an SMG at a redshift of 2.3259 (Swinbank et al. 2010; Negrello et al. 2010), and similar to the size of the dust emitting region found in Section 4.1. The corresponding beam filling fractions are listed in Table 4. As this source solid angle now represents the intrinsic size, and not the magnified one, we must correct the observed flux densities by the lensing magnification factors. We use the values listed in Table 2, when available, and assume a value of 10 in all other cases. The case of SDP.17a is treated differently, as it is assumed to be a foreground galaxy, not affected by gravitational lensing. For the intrinsic size of SDP.17a, we use a value of 1.54 arcsec 2 , which approximates the size of the optical image. Negrello et al. (2010) identify two galaxies in the i-band image of SDP.17 and fit both light distributions with the GALFIT software. As the presence of two galaxies could indicate a possible merger, we choose the source size of SDP.17a to be the sum of the areas of these two galaxies.

The distribution of the velocity-integrated brightness temperatures for the CO lines can be constructed starting from the CO column density and gas temperature, under the assumption of LTE. Following Goldsmith & Langer (1999), the velocity-integrated Rayleigh-Jeans source brightness is given by

$$W(J) = N_J \frac{hc^3 A_{J,J-1}}{8\pi k \nu^2} \frac{1 - e^{-\tau_{J,J-1}}}{\tau_{J,J-1}}, \quad (6)$$

where $\tau_{J,J-1}$ is the line center optical depth, and $A_{J,J-1}$ is the Einstein A coefficient for the transition. In LTE, the column density of molecules in the upper level, N_J , is related to the total column density N , by

$$N_J = \frac{N}{Z} g_J e^{-E_J/kT_{ex}}, \quad (7)$$

where Z is the partition function, E_J is the energy of level J , and $g_J = 2J + 1$ is the degeneracy of level J . The line center optical depth can be expressed as a function of column density, temperature, and line width Δv as

$$\tau_{J,J-1} = A_{J,J-1} \frac{c^3}{8\pi \nu^3 \Delta v} N_J (e^{h\nu/kT_{ex}} - 1). \quad (8)$$

We fit Equation 6 to the measured $W(J)$ distribution, with the column density and gas temperature as free parameters, and $\Delta v = 300 \text{ km s}^{-1}$. We find that the best fit models have relatively low optical depths ($\lesssim 1$) such that the choice of the line width has only a small effect on the fitted parameters. For the lensed galaxies, the measured CO SLEDs and the range of SLEDs allowed by the formal 1σ interval for the gas temperature are shown in Figure 9.

The SLEDs can be characterized by an overall scale and line ratios. The scale of the observed SLEDs is mainly a result of the CO column density and the beam filling fraction, while the line ratios depend on the CO temperature and gas (H_2) density. The parameters in each pair are therefore largely degenerate and anti-correlated. This degeneracy is characteristic to CO and other molecular SLEDs, regardless of galaxy type. The last correlation (between temperature and gas density) only exists until LTE is reached, and the temperature becomes fixed. By making assumptions on the beam filling fraction and gas density, we can place limits on the remaining parameters. The error bars on the column densities derived in this manner are correlated with the errors in the beam filling fraction, which are not known. Similarly, by making the assumption of LTE for all transitions up to CO (7-6), we are constraining the gas density to be greater than the critical density for this transition ($n[\text{H}_2] \gtrsim 3 \times 10^5 \text{ cm}^{-3}$). At densities $n[\text{H}_2] \gtrsim 10^6 \text{ cm}^{-3}$, considerably larger than the average value observed in Galactic molecular clouds, all observed lines should be in LTE. Values of the gas density more typical for Galactic molecular clouds ($10^3\text{-}10^4 \text{ cm}^{-3}$) correlate with higher gas temperatures, of a few hundred degrees, in order to reproduce the observed line ratios.

The best-fit LTE CO column densities are $\sim \text{few} \times 10^{18} \text{ cm}^{-2}$, and the gas temperature ranges between 41 and 115 K, as listed in Table 4. Taking into account the assumed source size, we estimate total CO masses of a $\text{few} \times 10^6 M_\odot$, only $\sim 10^{-4}$ of the total gas mass. Together with the large pressure associated with this model ($\sim 108 \text{ K cm}^{-3}$), this suggests that the LTE scenario can only describe a small portion of the gas. Other regions of the parameter space are associated with non-LTE gas excitation, explored with the RADEX modeling in the next section.

4.2.2. *Non-LTE radiative transfer models of CO line excitation*

In general, the rotational levels of the CO molecule might not be populated according to a single temperature, and the gas is not necessarily in equilibrium with the radiation field. By dropping the LTE assumption, we allow the excitation temperature to be a function of transition, being determined by the level populations for each line, while the kinetic

temperature will be the global quantity describing the thermal energy of the gas. The level populations are found by solving the detailed balance equations including both radiative and collisional rates, and the output intensities are calculated by solving the radiative transfer equations. Usually, these equations are strongly coupled, involving large spatial and frequency grids, and further complicated by the number of molecules and transitions involved. Simplifying assumptions are usually made to reduce the computing time, depending on the problem at hand.

We use RADEX to estimate the range of physical parameters consistent with the measured line strengths when dropping the LTE assumption. RADEX is a one dimensional, non-LTE radiative transfer code, that solves for the level populations iteratively, employing the escape probability approximation for the radiative transfer (van der Tak et al. 2007). The medium is assumed homogeneous and isothermal, and the number, type, and abundance of the participating molecules is selectable by the user. The input parameters are the kinetic temperature, T_{kin} , the number density of molecular hydrogen, $n[\text{H}_2]$, as the collisional partner, and the column densities per unit line width of the participating molecules, only CO in our case. The background radiation field is the CMB, redshifted according to the redshift of each galaxy. The output contains the predicted line excitation temperatures, optical depths, and line intensities. The output line fluxes are scaled by an additional factor ϕ , that represents fractional corrections to the size of the emitting region and to the gravitational lensing magnification factor. It would correspond to the area filling fraction of the emitting region, if the size and lensing magnification factor of the source were known precisely. A value $\phi > 1$ would suggest that the assumed source size was underestimated. We compare the measured flux densities with the line intensities output by RADEX using the values for source sizes, line widths, and lensing magnification factors assumed in Section 4.2.1 for the LTE model. For the case $\phi = 1$ and $n[\text{H}_2] \gg n_{crit}$ for all transitions, RADEX should recover the LTE SLED as determined from T_{ex} and $N[\text{CO}]$ in Section 4.2.1. This set of parameters represents the model m01, listed in Table 5 for each galaxy. The high $n[\text{H}_2]$ chosen for this model (10^6 cm^{-3}) insures that all measured lines will be in LTE. The SLED computed by RADEX for m01 is shown by the blue line in Figure 9, showing a good agreement with the LTE method described in the previous section.

We run RADEX for a range of input models, parametrized by T_{kin} , $N[\text{CO}]$, $n[\text{H}_2]$ and ϕ , and compute the likelihood density function for all models following the method described in Ward et al. (2003). Weak priors are set to rule out unphysical solutions, keeping the total molecular mass smaller than the dynamical mass, and the length of the CO column smaller than the physical size of the galaxy (Ward et al. 2003; Panuzzo et al. 2010). The dynamical mass cut-off is estimated choosing the line width of 300 km s^{-1} . We also impose a limit for the kinetic temperature at 3000 K, where collisional dissociation of CO starts to dominate,

weakly dependent on the gas density.

We map the surface of the likelihood distribution and determine the location of its maximum by running a Markov chain Monte Carlo (MCMC) algorithm, described in detail in Scott et al. (2010). The 2D marginal probability contours obtained from the MCMC algorithm are shown in Figures 10 and 11, with the position of the 4D maximum likelihood indicated by the dotted line, and the parameters of the m01 model, equivalent to the LTE solution, shown by the dashed lines. Note that due to projection effects the parameters corresponding to the maximum of the likelihood in the 4D parameter space are not necessarily the same as the coordinates of the maximum for the 2D marginal probability distributions. The set of parameters that maximizes the 4D likelihood for each galaxy is listed in Table 5 as model m02, and the line luminosities predicted by this model are shown in blue in Figure 9. The 68% credible regions are calculated as the smallest intervals containing 68% of the 1D marginal probability for each parameter, around the value corresponding to the 4D maximum likelihood. The 4D probability distributions are highly non-gaussian, and the maxima of the marginalized distributions are not a good representation of the true maximum of the 4D distribution.

Due to the aforementioned degeneracies (see Section 4.2.1), the product between the kinetic temperature and gas density on one hand, and CO column density and ϕ on the other hand, are better constrained than individual parameters. These products lead to the values for gas pressure and total gas mass listed in Table 5. Taking into account the lensing magnification factor, the inferred gas mass for non-LTE models is in good agreement with the mass derived from L'_{CO} (Table 4). The credible regions for ϕ suggest that the size of the emitting region could be larger than assumed for the LTE models, which would also correspond to a larger area characterized by lower gas density and pressure than the LTE case.

The properties of these models can be compared by calculating the *total* CO luminosity, summed over all transitions in the model, as a proxy for the indicators of the star formation rate and efficiency. The ratios L_{IR}/L'_{CO} for each model listed in Table 5 suggest that the star formation efficiency is higher for the LTE models. Using the correlation between total L_{CO} and L_{IR} derived for a mixed sample of nearby and high redshift galaxies by Bayet et al. (2009), we find that the total L_{CO} obtained by integrating the models will overpredict the measured L_{IR} in both cases, but are consistent within the scatter. The deviation between the predicted and measured L_{IR} is larger for model m02, slightly disfavoring this solution. While the LTE models tend to underpredict the total gas masses, the non-LTE models potentially underpredict the total infrared luminosity.

The region of the parameter space that is most consistent with the observed line

strengths is enclosed by the likelihood contours in Figures 10 and 11. We see that the LTE solution implies large gas densities ($n[\text{H}_2]$), as expected, but a class of non-LTE solutions can be found in the region defined by the likelihood contours in parameter space. The likelihood space roughly splits into high density/low temperature, and low density/high temperature solutions. One possible additional complication to the interpretation can arise from high dust optical depths Papadopoulos et al. (e.g., 2010), not included in our models, that can lead to the suppression of mid- J CO lines and to an underestimate of the excitation temperature. However, the likelihood distribution is relatively shallow over the whole region, reflecting the insufficient amount of information in our data. Comparatively, other studies of high redshift SMGs find a warm CO component with $n[\text{H}_2]$ around 10^4 cm^{-3} and temperatures between ~ 40 and 60 K (Riechers et al. 2010; Carilli et al. 2010; Danielson et al. 2010), a region marginally allowed by our contours.

The constraints on the parameter space for the non-LTE models are weak, as expected given the average sampling of the SLED, and cannot distinguish at this point between the LTE and non-LTE scenarios. To emphasize the insight gained by including additional lines in the fit, we add to the SLED of SDP.81 the CO(1-0) integrated flux from Frayer et al. (2010). A likelihood analysis for the new set of lines results in the best fit parameters listed in Table 5 as m03. The 2D marginalized likelihoods for this case are shown by the light grey contours in Figures 10 and 11. The tightening of the likelihood contours is substantial with just one line added to the data, and the LTE region of the parameter space becomes less favored. However, the limitation of this model is that it assumes a single gas component, while most of the emission in the CO(1-0) line could be originating from cold molecular gas.

The brightness temperatures predicted by the RADEX models m01 and m02 are shown in Figure 12, to emphasize the large deviations between the predictions of the two models, especially for lower J transitions. The measured data points have been scaled by the lensing magnification factors listed in Table 2 when available, and by a factor of 10 in all other cases. This figure shows that the constraints on the model parameters can be tightened by measurements of lower J transitions, especially the CO(1-0) line. Even if most of the CO(1-0) emission comes from a colder gas component, using this value as an upper limit will help rule out some regions of the parameter space, as in our example for SDP.81.

Distinguishing between the different regions in parameter space will clarify the state of the ISM in these galaxies, and thus their star formation histories. Specifically, hot/low-density gas may signal the action of a feedback process quenching further star formation, by increasing the Jeans mass. This high temperature/low density solution has not been fully investigated, but recent studies show that other CO SLEDs can be consistent with it (Panuzzo et al. 2010; Weiß et al. 2007; Ao et al. 2008; Bayet et al. 2009). The CO

SLED in M82 is fit by a small CO component with a kinetic temperature of almost 600 K (Panuzzo et al. 2010), while solutions with T_{kin} of a few $\times 100$ K are found by Bayet et al. (2009), and can be allowed by the LVG models for IRAS F10212+4724 (Ao et al. 2008) and APM 08279+5255 (Weiß et al. 2007). Such temperatures suggest energy input from outflows or AGN activity. The presence of an AGN component in SDP.17b is supported by the relatively flat SLED from CO(6-5) to CO(8-7), similar to the Cloverleaf quasar or Mrk231 (Bradford et al. 2009; Van der Werf et al. 2010), and the emission line of water, also observed in galaxies with an AGN component, such as Mrk231 (González-Alfonso et al. 2010).

5. CONCLUSIONS

Far-IR / submillimeter-wave surveys are revealing submillimeter-bright galaxies from the first half of the Universe by the tens of thousands, but their detailed study requires spectroscopic redshift measurements. We have studied a sample of the brightest sources and have demonstrated a new redshift-measurement technique with our broadband millimeter-wave grating spectrometer, Z-Spec. Z-Spec measures multiple rotational transitions of carbon monoxide, the dominant coolant of molecular gas in galaxies, and thus is not dependent on optical counterparts which are often absent or hard to identify, as is the case for these galaxies. We find redshifts ranging roughly between 1 and 3, in line with previous determinations (Chapman et al. 2005), reaching back to an era when the Universe was 15% its present age. Their fluxes are proven to be amplified by gravitational lensing (Negrello et al. 2010), making them ideal targets for spectroscopic follow-ups. From the observed CO line luminosities and integrated L_{IR} , typical conversion factors reveal that these galaxies each house roughly $10^{10} M_{\odot}$ of molecular gas, and have SFRs between 10^2 and $10^3 M_{\odot} \text{yr}^{-1}$, after correcting for lensing magnification. Regardless of the magnification details, we are clearly witnessing a rare episode of rapid star formation in these galaxies, since the timescale over which the observed luminosity can be generated by converting the inferred mass of gas into stars is only a few tens of millions of years (depending on the details of the star formation and the accretion of more gas), which is a small fraction of the Universe's age even at this early epoch. We estimate that the dust masses in our sample of lensed galaxies are around a few $\times 10^8 M_{\odot}$, and the wavelengths corresponding to the peaks of their dust SEDs fall within a narrow range, between 73 and 92 μm in the rest frame. For this initial set of lensed submm galaxies both the dust properties derived from the IR SED, and the physical conditions of the molecular gas probed by the CO lines, are broadly comparable to those in known SMGs (Greve et al. 2005; Solomon & Vanden Bout 2005; Casey et al. 2009), with excitation temperatures in the 30-120 K range, and L'_{CO}/L_{IR} between 1 and $3 \times 10^{-3} \text{ K km s}^{-1} \text{ pc}^2/L_{\odot}$, as

measured from the mid- J CO lines.

The partial SLEDs for the CO molecule constructed from the lines observed by Z-Spec cannot distinguish between different models of CO excitation. The simplest assumption is that of local thermodynamic equilibrium (LTE), under which we can derive the gas column density and excitation temperature. We find that the relative line strengths can be reproduced by relatively low excitation temperatures (< 100 K), and optical depths (< 1). In the non-LTE case, other parts of the parameter space are allowed, including higher optical depths, while measurements of the lower rotational transitions are essential in confirming such models.

By being able to characterize galaxies that can be inaccessible at other wavelengths, the combination of large-area submm surveys and spectroscopic follow-ups of the CO emission lines will lead to substantial progress in our understanding of high redshift galaxies and their evolution. These results suggest the possibility of a rapid growth in our understanding of SMGs, independent of their optical or radio counterparts, but enabled by strong gravitational lensing magnification.

We are indebted to the staff of the Caltech Submillimeter Observatory for their unflagging support. This work was supported by NSF grant AST-0807990 to J. Aguirre and by the CSO NSF Cooperative Agreement AST-0838261. Support was provided to J. Kamenetzky by an NSF Graduate Research Fellowship. Z-spec was constructed under NASA SARA grants NAGS-11911 and NAGS-12788 and an NSF Career grant (AST-0239270) and a Research Corporation Award (RI0928) to J. Glenn, in collaboration with the Jet Propulsion Laboratory, California Institute of Technology, under a contract with the National Aeronautics and Space Administration. We acknowledge Peter Ade and his group for their filters and Lionel Duband for the $3\text{He} / 4\text{He}$ refrigerator in Z-Spec, and are grateful for their help in the early integration of the instrument. R. L. wishes to thank Tom Loredó for useful discussions regarding the significance of the redshift determination. We appreciate the help of Robert Hanni and Jon Rodríguez with observing.

REFERENCES

- Amblard, A., et al. 2010, *A&A*, 518, L9+
- Ao, Y., Weiß, A., Downes, D., Walter, F., Henkel, C., & Menten, K. M. 2008, *A&A*, 491, 747
- Aravena, M., et al. 2010, *ApJ*, 718, 177

- Aretxaga, I., et al. 2007, MNRAS, 379, 1571
- Austermann, J. E., et al. 2010, MNRAS, 401, 160
- Bayet, E., Gerin, M., Phillips, T. G., & Contursi, A. 2009, MNRAS, 399, 264
- Bertoldi, F., et al. 2007, ApJS, 172, 132
- Blain, A. W. 1999, MNRAS, 309, 955
- Blain, A. W., Smail, I., Ivison, R. J., Kneib, J.-P., & Frayer, D. T. 2002, Phys. Rep., 369, 111
- Bradford, C. M., et al. 2009, ApJ, 705, 112
- Carilli, C. L., et al. 2010, ApJ, 714, 1407
- Casey, C. M., et al. 2009, ArXiv e-prints
- Chapman, S. C., Blain, A. W., Smail, I., & Ivison, R. J. 2005, ApJ, 622, 772
- Chary, R., & Elbaz, D. 2001, ApJ, 556, 562
- Clements, D. L., et al. 2010, A&A, 518, L8+
- Coppin, K., et al. 2006, MNRAS, 372, 1621
- da Cunha, E., Charlot, S., & Elbaz, D. 2008, MNRAS, 388, 1595
- Daddi, E., et al. 2009, ApJ, 695, L176
- Dale, D. A., & Helou, G. 2002, ApJ, 576, 159
- Danielson, A. L. R., et al. 2010, ArXiv e-prints
- Devriendt, J., et al. 2010, MNRAS, 403, L84
- Dunne, L., Eales, S., Edmunds, M., Ivison, R., Alexander, P., & Clements, D. L. 2000, MNRAS, 315, 115
- Eales, S., et al. 2010, PASP, 122, 499
- Earle, L., et al. 2006, in Presented at the Society of Photo-Optical Instrumentation Engineers (SPIE) Conference, Vol. 6275, Society of Photo-Optical Instrumentation Engineers (SPIE) Conference Series

- Frayer, D. T., Ivison, R. J., Scoville, N. Z., Yun, M., Evans, A. S., Smail, I., Blain, A. W., & Kneib, J. 1998, *ApJ*, 506, L7
- Frayer, D. T., et al. 2010, ArXiv e-prints
- Goldsmith, P. F., & Langer, W. D. 1999, *ApJ*, 517, 209
- González-Alfonso, E., et al. 2010, ArXiv e-prints
- Greve, T. R., et al. 2005, *MNRAS*, 359, 1165
- Griffin, M. J., et al. 2010, ArXiv e-prints
- Harris, A. I., Baker, A. J., Zonak, S. G., Sharon, C. E., Genzel, R., Rauch, K., Watts, G., & Creager, R. 2010, ArXiv e-prints
- Hughes, D. H., Robson, E. I., Dunlop, J. S., & Gear, W. K. 1993, *MNRAS*, 263, 607
- Hughes, D. H., et al. 2002, *MNRAS*, 335, 871
- Ibar, E., et al. 2010, ArXiv e-prints
- Inami, H., et al. 2008, in Presented at the Society of Photo-Optical Instrumentation Engineers (SPIE) Conference, Vol. 7020, Society of Photo-Optical Instrumentation Engineers (SPIE) Conference Series
- Ivison, R. J., Papadopoulos, P. P., Smail, I., Greve, T. R., Thomson, A. P., Xilouris, E. M., & Chapman, S. C. 2010a, ArXiv e-prints
- Ivison, R. J., et al. 2010b, ArXiv e-prints
- Knudsen, K. K., Neri, R., Kneib, J., & van der Werf, P. P. 2009, *A&A*, 496, 45
- Kovács, A., Chapman, S. C., Dowell, C. D., Blain, A. W., Ivison, R. J., Smail, I., & Phillips, T. G. 2006, *ApJ*, 650, 592
- Lestrade, J., Combes, F., Salomé, P., Omont, A., Bertoldi, F., André, P., & Schneider, N. 2010, ArXiv e-prints
- Low, F. J., & Tucker, W. H. 1968, *Physical Review Letters*, 21, 1538
- Michałowski, M. J., Watson, D., & Hjorth, J. 2010, *ApJ*, 712, 942
- Naylor, B. J., et al. 2003, in Presented at the Society of Photo-Optical Instrumentation Engineers (SPIE) Conference, Vol. 4855, Society of Photo-Optical Instrumentation Engineers (SPIE) Conference Series, ed. T. G. Phillips & J. Zmuidzinas, 239–248

- Negrello, M., et al. 2007, MNRAS, 377, 1557
- . 2010, Science, in press
- Neri, A., et al. 2010, in preparation
- Panuzzo, P., et al. 2010, ArXiv e-prints
- Papadopoulos, P. P., van der Werf, P., Isaak, K., & Xilouris, E. M. 2010, ApJ, 715, 775
- Pascale, E., et al. 2008, ApJ, 681, 400
- . 2010, in preparation
- Pilbratt, G. L., et al. 2010, A&A, 518, L1+
- Poglitsch, A., et al. 2010, A&A, 518, L2+
- Priddey, R. S., & McMahon, R. G. 2001, MNRAS, 324, L17
- Puget, J., Abergel, A., Bernard, J., Boulanger, F., Burton, W. B., Desert, F., & Hartmann, D. 1996, A&A, 308, L5+
- Riechers, D. A., et al. 2010, ApJ, 720, L131
- Rigby, E., et al. 2010, in preparation
- Santini, P., et al. 2010, A&A, 518, L154+
- Scott, K. S., et al. 2008, MNRAS, 385, 2225
- . 2010, in preparation
- Silk, J., & Spaans, M. 1997, ApJ, 488, L79+
- Smail, I., Ivison, R. J., & Blain, A. W. 1997, ApJ, 490, L5
- Soifer, B. T., & Neugebauer, G. 1991, AJ, 101, 354
- Solomon, P. M., Downes, D., Radford, S. J. E., & Barrett, J. W. 1997, ApJ, 478, 144
- Solomon, P. M., & Vanden Bout, P. A. 2005, ARA&A, 43, 677
- Spergel, D. N., et al. 2007, ApJS, 170, 377
- Swinbank, A. M., et al. 2010, Nature, 464, 733

Tacconi, L. J., et al. 2008, *ApJ*, 680, 246

van der Tak, F. F. S., Black, J. H., Schöier, F. L., Jansen, D. J., & van Dishoeck, E. F. 2007, *A&A*, 468, 627

Van der Werf, P. P., et al. 2010, ArXiv e-prints

Vieira, J. D., et al. 2009, ArXiv e-prints

Wang, R., et al. 2010, *ApJ*, 714, 699

Ward, J. S., Zmuidzinas, J., Harris, A. I., & Isaak, K. G. 2003, *ApJ*, 587, 171

Weiß, A., Downes, D., Neri, R., Walter, F., Henkel, C., Wilner, D. J., Wagg, J., & Wiklind, T. 2007, *A&A*, 467, 955

Weiss, A., Downes, D., Walter, F., & Henkel, C. 2007, in *Astronomical Society of the Pacific Conference Series*, Vol. 375, *From Z-Machines to ALMA: (Sub)Millimeter Spectroscopy of Galaxies*, ed. A. J. Baker, J. Glenn, A. I. Harris, J. G. Mangum, & M. S. Yun, 25–+

Weiss, A., Ivison, R. J., Downes, D., Walter, F., Cirasuolo, M., & Menten, K. M. 2009a, *ApJ*, 705, L45

Weiss, A., et al. 2009b, *ApJ*, 707, 1201

Wright, E. L. 2007, ArXiv Astrophysics e-prints

Table 1. Summary of the Z-Spec observations on the H-ATLAS sources.

IAU Name	H-ATLAS SDP ID	Dates Observed	$\tau_{225\text{GHz}}$ (zenith)	Integration Time (hrs)	rms Uncertainty ^(a) (mJy)
H-ATLAS J090740.0-004200	SDP.9	Apr 27 - May 14	0.05 – 0.21	10.6	4.0
H-ATLAS J091043.1-000322	SDP.11	Apr 28 - May 4	0.05 – 0.18	6.8	5.5
H-ATLAS J090302.9-014128	SDP.17	Mar 28 - Apr 1	0.04 – 0.08	18.2	2.9
H-ATLAS J090311.6+003905	SDP.81	Mar 7 - Mar 12	0.02 – 0.05	22.5	2.3
H-ATLAS J091304.9-005344	SDP.130	Mar 21 - Mar 22	0.04 – 0.08	8.6	4.4

Note. — The columns list: 1) the IAU source identification; 2) the ID of the source in the SDP H-ATLAS catalogue; 3) the range of dates for the observations; 4) the range in $\tau_{225\text{GHz}}$ over all observations of the source; 5) the total integration time on the source (including the time spent in the off-source position during the nod cycle, but excluding all other overheads); and 6) the median rms uncertainty on the measured flux density.

^(a)Varies with frequency. The channel width is frequency dependent, with a mean of 950 km s^{-1} .

Table 2. Summary of the H-ATLAS galaxy sample and the parameters derived from fitting their submm SEDs.

H-ATLAS SDP ID	μ	z	Significance (p-value)	μL_{IR} ($10^{13} L_{\odot}$)	$T_d^{(d)}$ (K)	α	$\mu M_{d,lim}^{(e)}$ ($10^9 M_{\odot}$)	$\mu \Omega_d^{(e)}$ (arcsec ²)	μSFR ($10^3 M_{\odot}/yr$)
SDP.9	...	1.577±0.008	1.1e-11	4.4±0.6	57±1	3.8±0.2	2.5	0.65	6.6±0.9
SDP.11	...	1.786±0.005	3.1e-8	7.8±0.9	69±1	5.7±0.4	1.7	0.43	11.7±1.4
SDP.17a ^(a)	...	0.942±0.004	1.0e-4	0.4±0.1	27±1	2.9±0.1	4.9	1.44	0.6±0.2
SDP.17b ^(a)	...	2.308±0.011	1.9e-7	3.9±1.0	66±1	2.9±0.1	1.1	0.30	5.8±1.5
SDP.81	18-31 ^(b)	3.037±0.010	6.7e-5	6.4±0.3	58±1	3.2±0.1	2.2	0.69	9.6±0.5
SDP.130	5-7 ^(b)	2.626±0.0003 ^(c)	N/A	4.3±0.2	55±1	2.7±0.3	1.6	0.47	6.5±0.3

Note. — The columns list: 1) the ID of the source in the SDP H-ATLAS catalogue; 2) the gravitational lensing magnification factor; 3) the measured redshift; 4) the redshift significance, listed as the p-value, the probability that the null statistic would be larger than the maximum of the test statistic for the corresponding spectrum; 5) the integrated IR luminosity, obtained as the average between the SED fits with the CE01 libraries and the DH02 libraries. The factor μ is shown in front of quantities affected by gravitational lensing magnification; 6) the dust temperature; 7) the index of the power-law continuum fit to Z-Spec data; 8) the dust mass; 9) the solid angle subtended by the dust emitting region; and 10) the star formation rate.

^(a)The total observed flux was split between the two components, using a frequency-independent scale factor.

^(b)Values taken from Negrello et al. (2010).

^(c)Redshift determined by GBT/Zspectrometer, followed by a more precise measurement with PdBI/IRAM (Negrello et al. 2010).

^(d)The uncertainties for T_d are likely underestimated. The values shown are formal errors from the fit, and don't include correlations between parameters, or the inaccuracy of the assumed shape of the SED model. The values for β and ν_0 are kept fixed for all sources.

^(e)Calculated in the optically thin limit. The dust masses should be interpreted as robust lower limits for the true total

dust mass in the galaxy.

Table 3. Integrated fluxes for the emission lines identified in each galaxy.

Line	Frequency (GHz)	Integrated Line Flux (Jy km s ⁻¹)				
		SDP.9	SDP.11	SDP.17a	SDP.17b	SDP.81
CO (4-3)	461.041	15±9
CO (5-4)	576.268	25±5	23±8	29±9 ^(b)
CO (6-5)	691.473	33±7	29±10	...	17±5	...
CO (7-6)	806.652	...	18±14 ^(a)	...	11±7 ^(a)	12±4 ^(a)
CO (8-7)	921.800	16±6	5±3
CO (9-8)	1036.91	6±3
CO (10-9)	1151.99	< 6.5
[C I] ³ P ₁ → ³ P ₀	492.160	< 11	...	< 6
[C I] ³ P ₂ → ³ P ₁	809.342	...	31±14 ^(a)	...	13±7 ^(a)	< 6.5 ^(a)
H ₂ O 2 _{0,2} - 1 _{1,1}	987.914	19±7 ^(b)	...

Note. — The columns list: 1) the transition; 2) the rest frame frequency of the transition; and 3) the integrated line flux for each galaxy with 68% confidence intervals. Upper limits are 3σ .

^(a)These lines originate in the same source and are blended at the Z-Spec resolution. The error bars account for this uncertainty.

^(b)In the spectrum of SDP.17, the water line at $z=2.308$ and the CO(5-4) line at $z=0.94$ are blended.

Table 4. Derived starburst properties and LTE parameters for the H-ATLAS galaxy sample.

H-ATLAS SDP ID	$\mu L'_{CO}$ (10^{10} K km s $^{-1}$ pc 2)	$\mu M_{gas}^{(a)}$ (10^{11} M $_{\odot}$)	$t_{SF}^{(a)}$ (10^7 yr)	$N_{CO}^{(b)}$ (10^{17} cm $^{-2}$)	$T_{ex}^{(c)}$ (K)	$\Omega_s/\Omega_a^{(b)}$ (10^{-3})	τ_{CO}	$M_{CO}^{(d)}$ (10^6 M $_{\odot}$)
SDP.9	13 \pm 3	1.7	2.6	19 \pm 4	76 \pm 24	0.3	0.251	1.4 \pm 0.3
SDP.11	15 \pm 5	2.0	1.7	47 \pm 14	41 \pm 6	0.3	0.983	3.5 \pm 1
SDP.17a	4 \pm 3	0.5	8.3	2.3 \pm 0.7	114 \pm 99	1.3	0.015	0.17 \pm 0.05
SDP.17b	12 \pm 3	1.6	2.8	19 \pm 6	65 \pm 10	0.3	0.298	1.4 \pm 0.4
SDP.81	10 \pm 3	1.3	1.4	11 \pm 3	53 \pm 5	0.6	0.149	0.8 \pm 0.2

Note. — The columns list: 1) the ID of the source in the SDP H-ATLAS catalogue; 2) the integrated brightness temperature of the lowest J CO transition measured, times the source area; 3) the molecular gas mass; 4) the gas depletion time; 5) the CO column density; 6) the CO excitation temperature under LTE; 7) the estimated beam filling fraction for the lowest J transition measured; 8) the optical depth for the lowest J transition measured in that source. The parameters in the last four columns have been derived in the LTE approximation; and 9) estimated total mass of CO gas.

^(a)The errors for these parameters depend mostly on the uncertainties in the assumed conversion factors (see Section 4.2).

^(b)These quantities are anti-correlated in the optically thin regime: larger CO column densities correspond to smaller beam filling fractions. The values displayed correspond to an intrinsic source diameter of ~ 2 kpc. The listed errors reflect the uncertainties in the measured integrated line fluxes. Other errors for this parameter, aside from the LTE model assumption, depend on our knowledge of the true source size.

^(c)The formal errors bars underestimate the uncertainty in T_{ex} , due to model assumptions restricted to LTE. In non-LTE models, a large region of the parameter space is allowed, and T_{ex} becomes J -dependent (see Section 4.2.2).

^(d)Corresponds to the assumed source radius of 1 kpc.

Table 5. Parameters used for the RADEX models shown in Figures 9 and 12.

RADEX Model	T_{kin} (K)	$\log(N_{CO})$ (10^{18} cm^{-2})	$\log(n[\text{H}_2])$ (cm^{-3})	ϕ	$\log(P)$ (K cm^{-3})	$\log(M_{gas})$ (M_{\odot})	$L_{IR}/L'_{CO,total}$
SDP.9							
m01 ^(a)	76.	18.27	6.20	1.00	8.1	8.8	55
m02 ^(b)	2628.	20.50	3.37	0.05	6.8	9.7	29
68% credible region ^(c)	149-2631	19.03-21.10	3.37-6.06	0.03-0.58	6.29-8.64	8.71-10.14	12-114
SDP.11							
m01	41.	18.67	6.20	1.00	7.8	9.2	78
m02	21.	19.74	6.50	1.66	7.8	10.5	67
68% credible region	21-611	18.42-20.17	3.61-6.55	0.19-1.82	5.85-7.83	9.14-10.50	27-520
SDP.17b							
m01	63.	18.32	6.20	1.00	8.0	8.8	55
m02	1988.	20.03	1.99	0.85	5.3	10.5	21
68% credible region	136-1992	19.11-21.03	1.99-5.14	0.04-1.02	5.29-7.59	8.93-10.51	0-626
SDP.81							
m01	53.	18.04	6.20	1.00	7.9	8.6	71
m02	213.	20.33	2.63	0.38	5.0	10.4	25
68% credible region	63-855	18.53-20.43	2.55-5.17	0.05-1.12	4.95-7.24	8.44-10.44	8-640
m03 ^(d)	481.	16.71	3.20	130.	5.89	9.35	18
68% credible region	368-2749	14.85-17.08	2.56-3.42	35-6600	5.80-6.04	9.22-9.43	12-55

Note. — The columns list: 1) the model notation; 2) the kinetic temperature T_{kin} (under LTE, $T_{kin}=T_{ex}$); 3) the CO column density; 4) the density of H_2 ; 5) ϕ is an overall scaling factor, that would correspond to the area filling fraction if the intrinsic source size and gravitational lensing magnification factor were known exactly. This enters as the fourth unknown parameter in the maximum likelihood estimation; 6) the gas pressure; 7) the total gas mass in the beam; and 8) the $L_{IR}/L'_{CO,total}$ as a measure of the star formation efficiency predicted by each model, where L'_{CO} is summed over all CO transitions in the model.

^(a)The parameters used for model m01 correspond to the best fit LTE solution in Table 4. This requirement translates into fixed values for $n[\text{H}_2]$ and ϕ . The errors for the other parameters can be also found in Table 4.

^(b)The parameters of model m02 correspond to the 4D maximum likelihood solution from an MCMC exploration of the parameter space with 10^5 iterations for each galaxy. Additional measured CO transitions would help rule out solutions with extreme temperatures and densities.

^(c)This represents the smallest interval enclosing 68% of the *marginal* probability for each parameter.

^(d)The third model for SDP.81 includes the CO(1-0) measurement from Frayer et al. (2010).

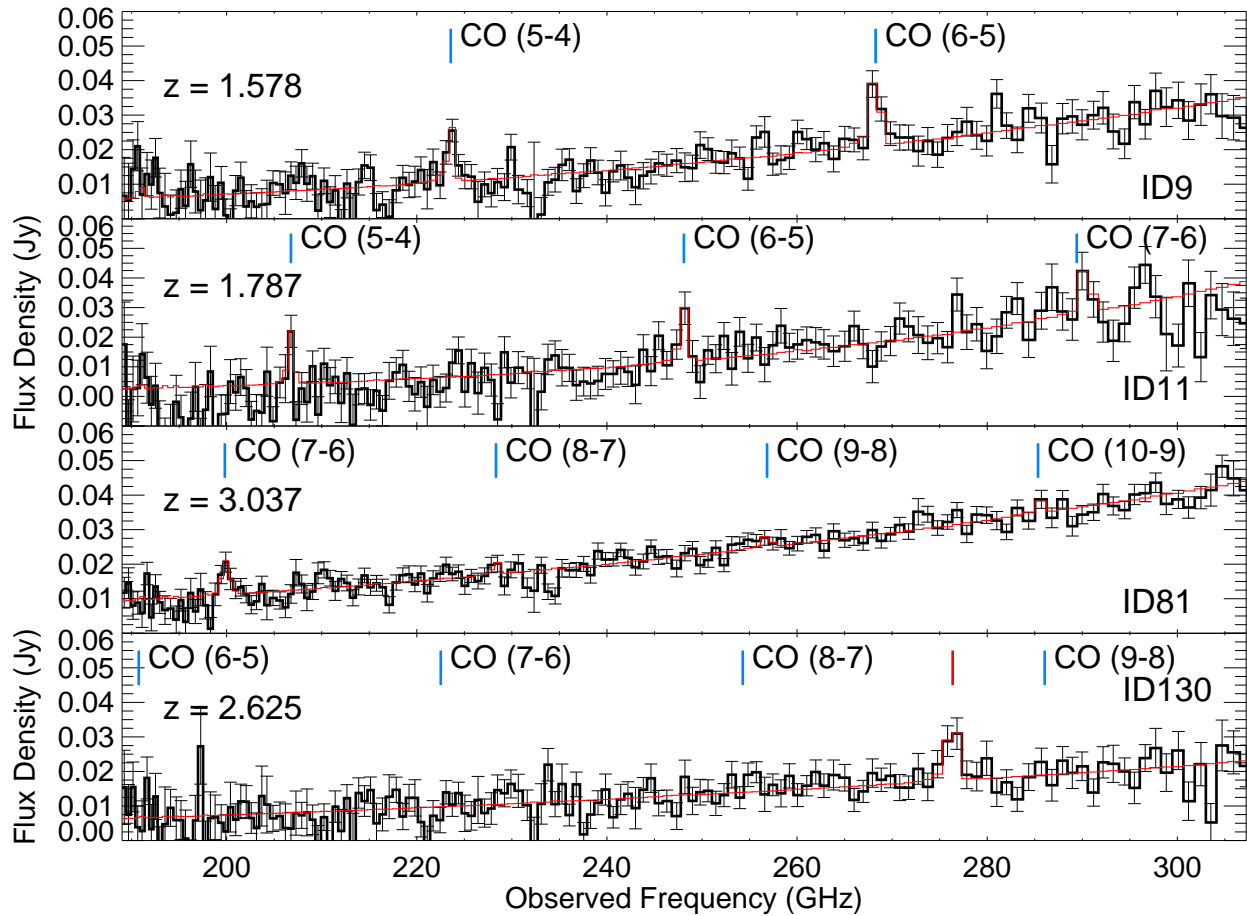


Fig. 1.— The Z-Spec spectra of four submillimeter bright H-ATLAS galaxies. The fit to the continuum and CO lines at the measured redshift is overplotted in red, and the positions of the strongest lines falling in the Z-Spec bandpass are indicated by the vertical blue lines. The line indicated in red in the spectrum of SDP.130 is unidentified.

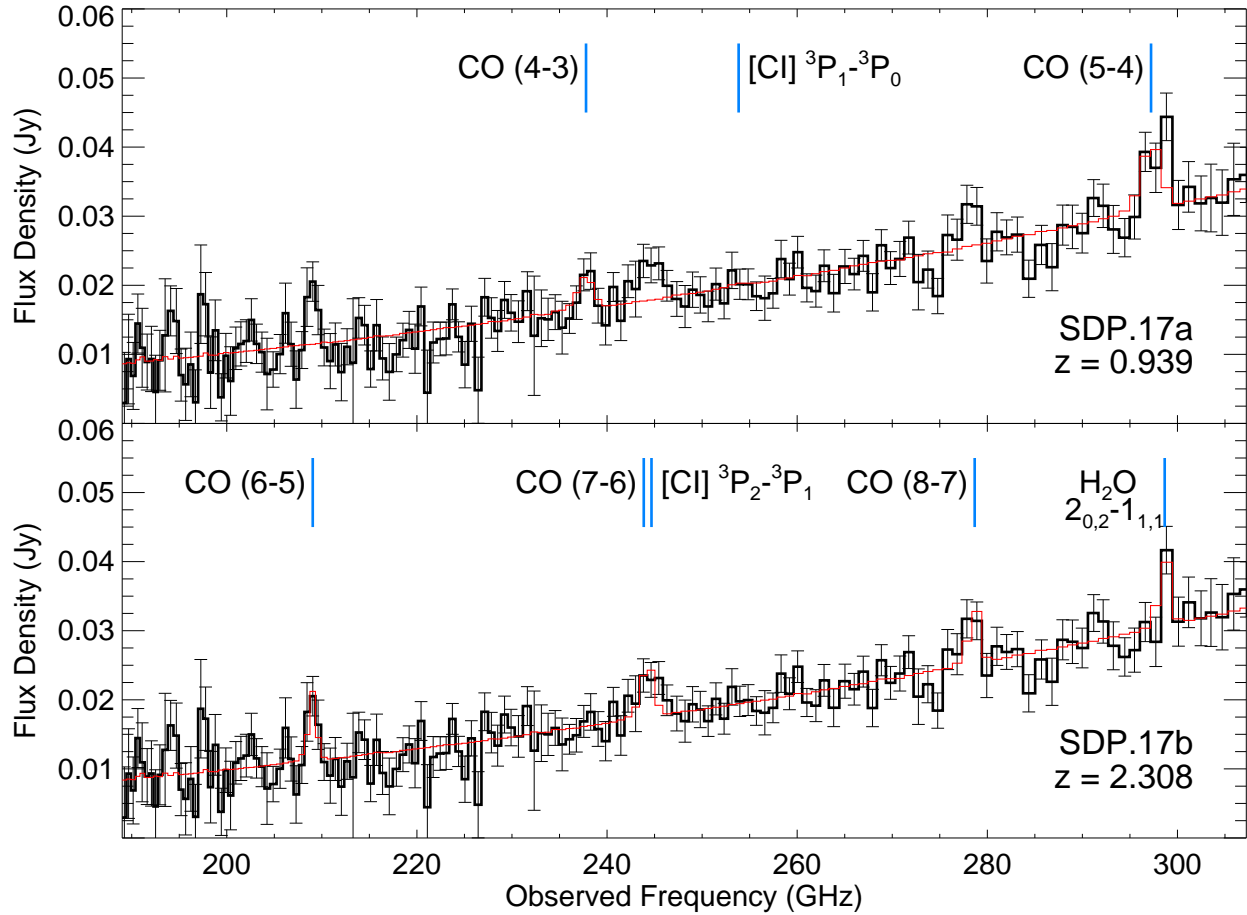


Fig. 2.— The Z-Spec spectrum of the H-ATLAS source SDP.17. The fit to the continuum and CO lines at $z = 0.94$ is overplotted in red in the upper panel, and the rotational CO lines are indicated by the vertical blue lines. These lines have been subtracted from the spectrum shown in the lower panel. The red line in the lower panel shows the fit including the lines identified at $z = 2.308$.

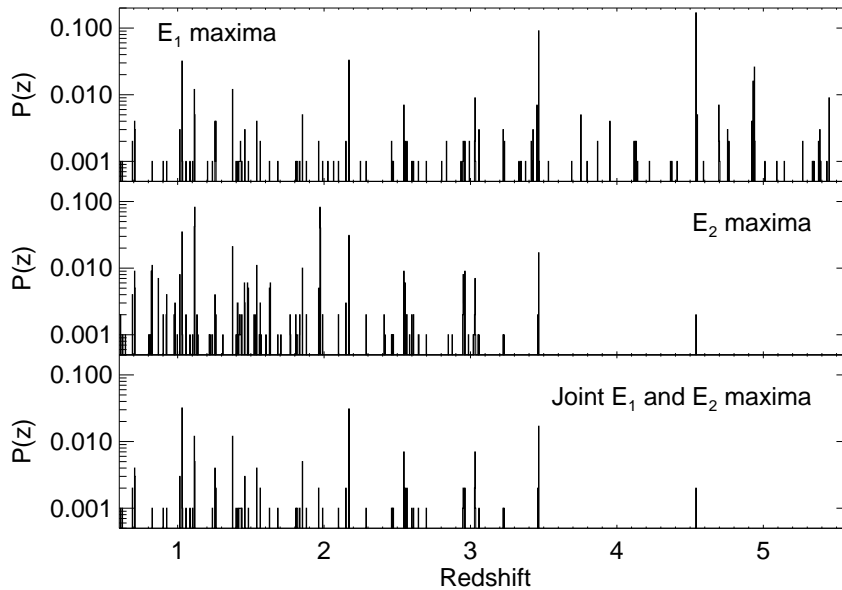


Fig. 3.— Blank sky probability distributions for the positions of the E_1 and E_2 maxima as a function of redshift. The redshift bin size is 0.003, corresponding to the average width of the Z-Spec channels. These probabilities have been obtained by running the redshift finding algorithm on 1000 realizations of the blank sky spectrum. The highest probability corresponds to the redshift most likely to be determined by each statistic. The last panel shows the probability distribution when the same redshift is found jointly by E_1 and E_2 . The maximum probability that a false positive is obtained simultaneously by the two test statistics is $\sim 3\%$.

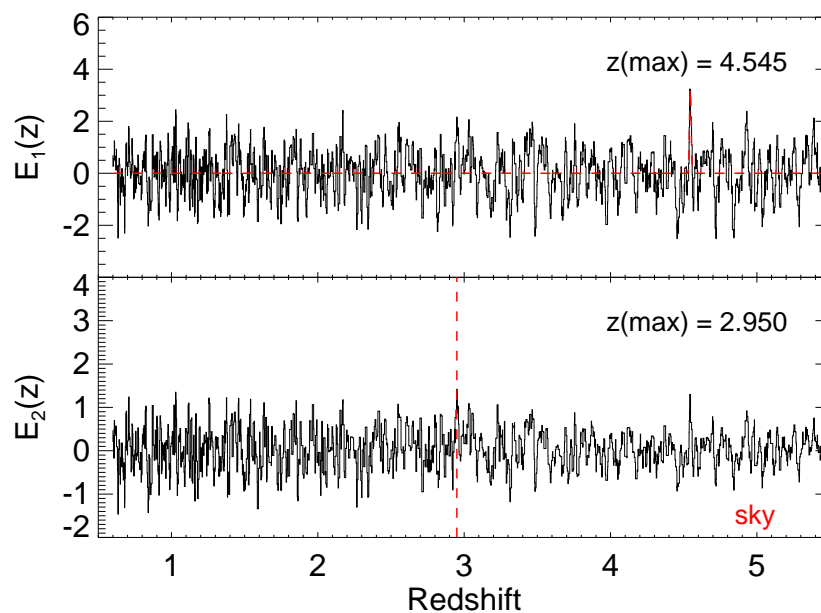


Fig. 4.— Null test for the redshift finding algorithm, using a blank sky spectrum. Note that the values of the E_2 test statistic are systematically below 1.5, and the positions of the maxima of the two test statistics do not coincide.

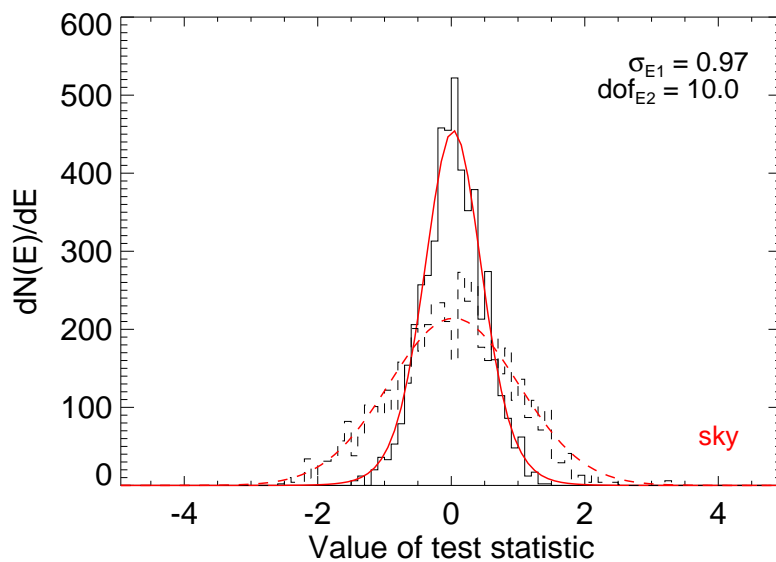


Fig. 5.— Distributions of the two test statistics derived from blank sky spectra. The histograms for E_1 and E_2 are shown with a dashed and continuous line, respectively. The fits with a normal distribution for E_1 and a t distribution for E_2 are overlotted as the smooth red curves.

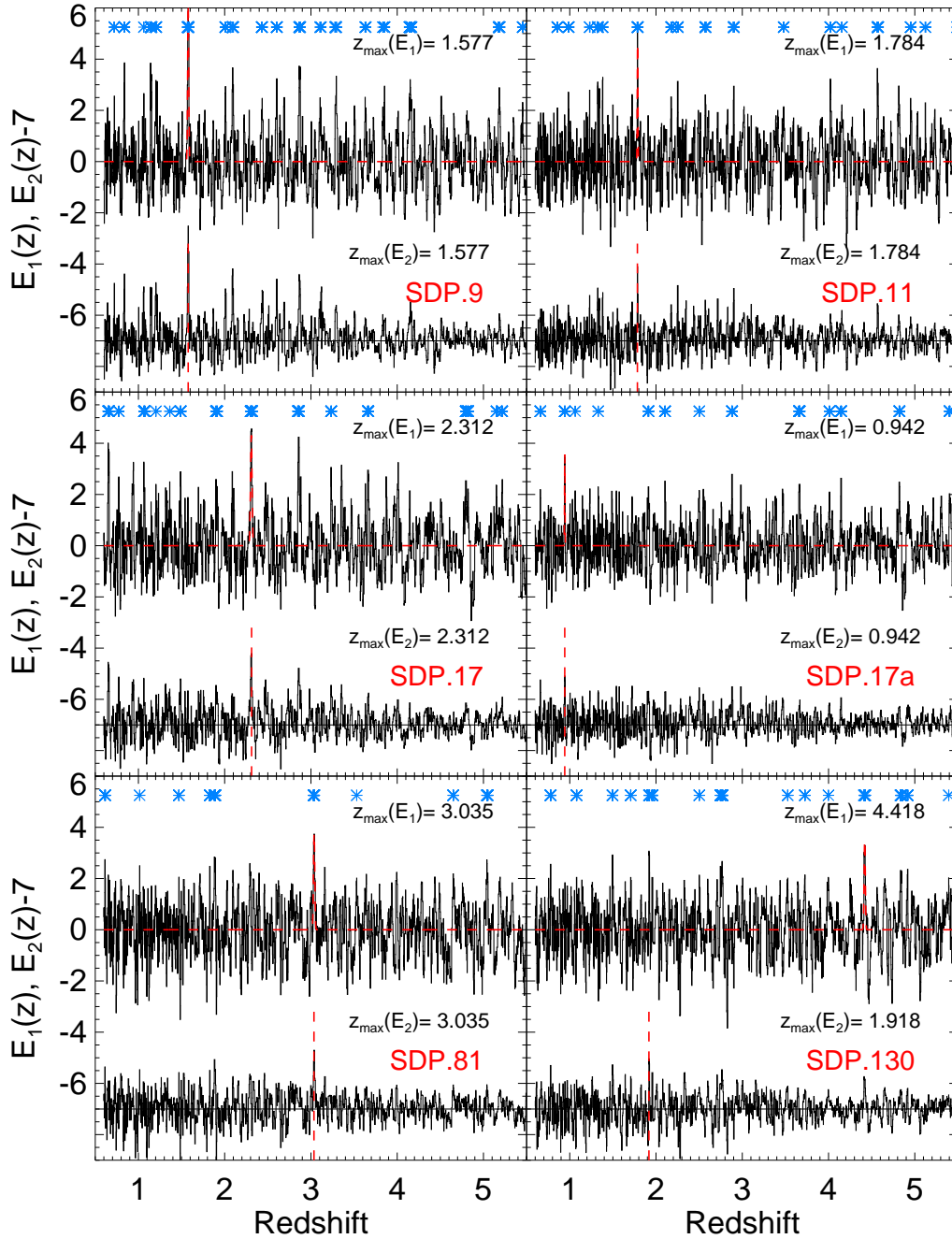


Fig. 6.— Results of running the redshift-finding algorithm for all the H-ATLAS sources in our sample. The E_2 test statistic has been offset vertically by 7 units, for clarity. The blue asterisks show the positions of the largest secondary peaks arising from coincidences with the lines from the actual redshift (see text). These peaks contain the same information as the main peak. In the SDP.17 panel, we note the extra peaks that do not match the secondary peaks corresponding to the first selected redshift. The SDP.17a panel shows the determination of the second redshift from the same spectrum, after subtracting the high-redshift component. No redshift is determined for SDP.130.

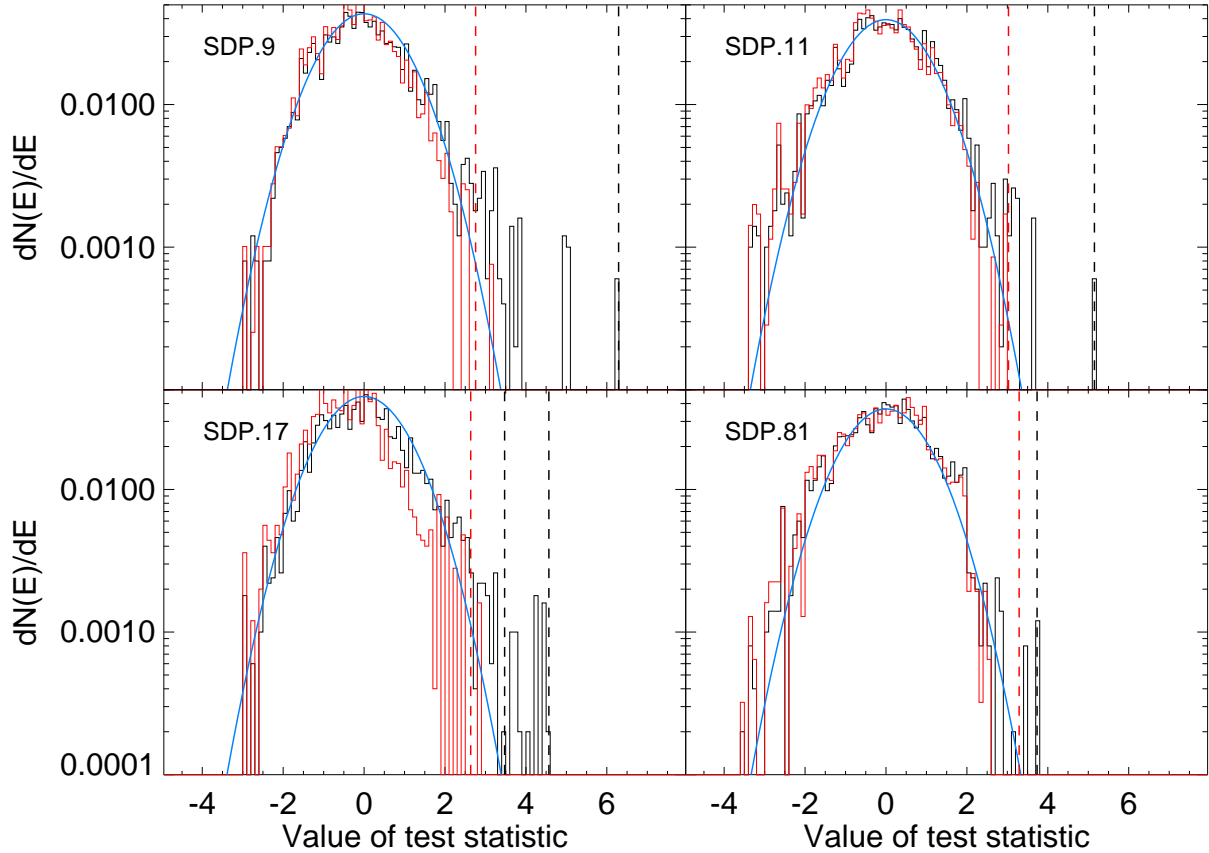


Fig. 7.— E_1 distribution for each galaxy for which we determined the redshift. The original E_1 distribution is shown in black, the red distribution being obtained after subtracting the main peak of E_1 and all its secondary peaks. The normal distribution fit to the null E_1 distribution is shown in blue. The red dashed line shows the 3σ position for the null gaussian, and the black dashed lines show the positions of the maximum of the test statistic for the measured redshifts, to emphasize the significance of our detections.

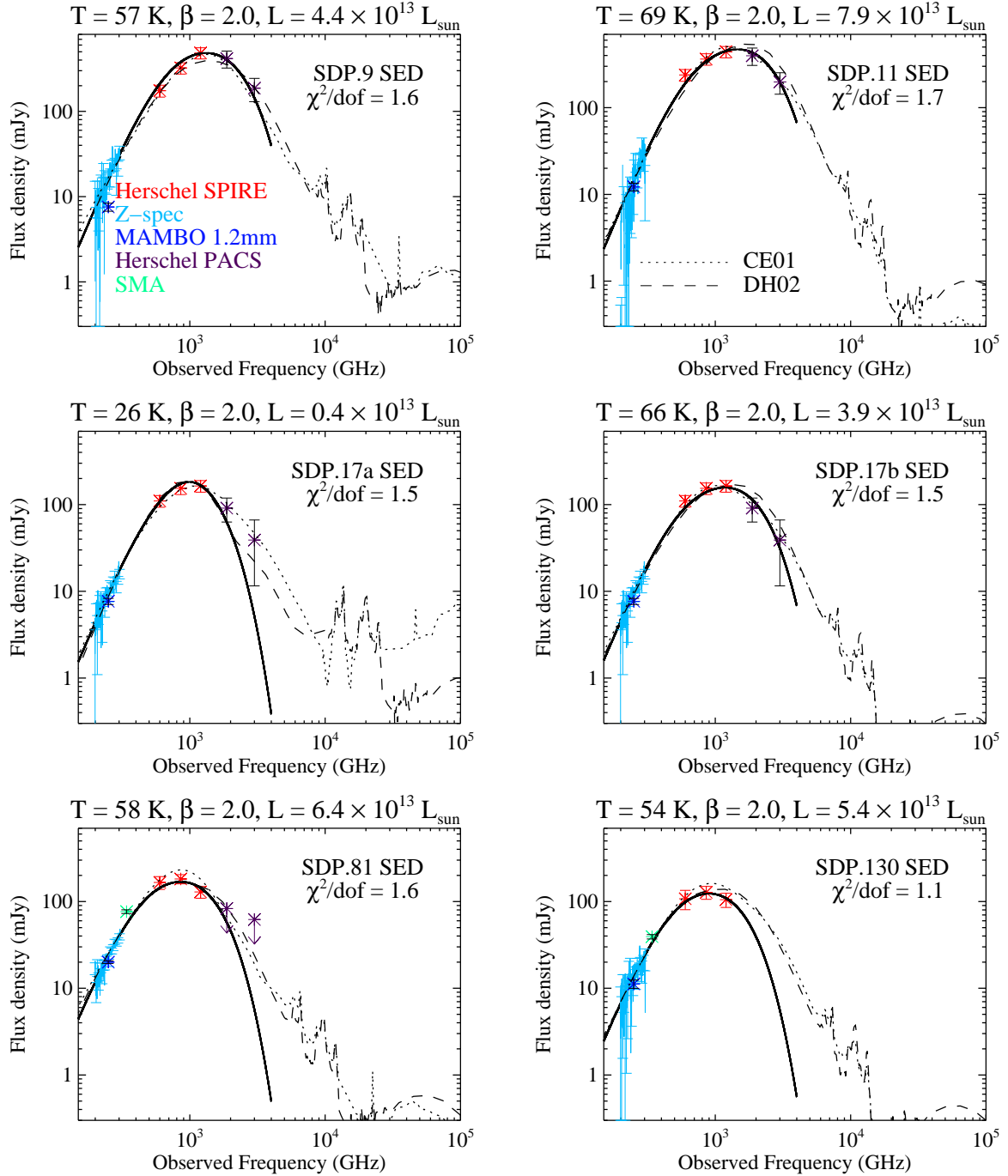


Fig. 8.— The best-fit SED models for the five H-ATLAS galaxies in our sample. The continuous line shows the modified blackbody spectrum with $\nu_0 = 1300$ GHz and $\beta = 2.0$, while the dotted and dashed lines show the SEDs obtained from the SED libraries of CE01 and DH02, respectively. The total infrared luminosities are calculated as the average between the CE01 and DH02 SED template fits, to account for emission above the blackbody spectrum at higher frequencies. The parameters for the modified blackbody fits are also listed in Table 2.

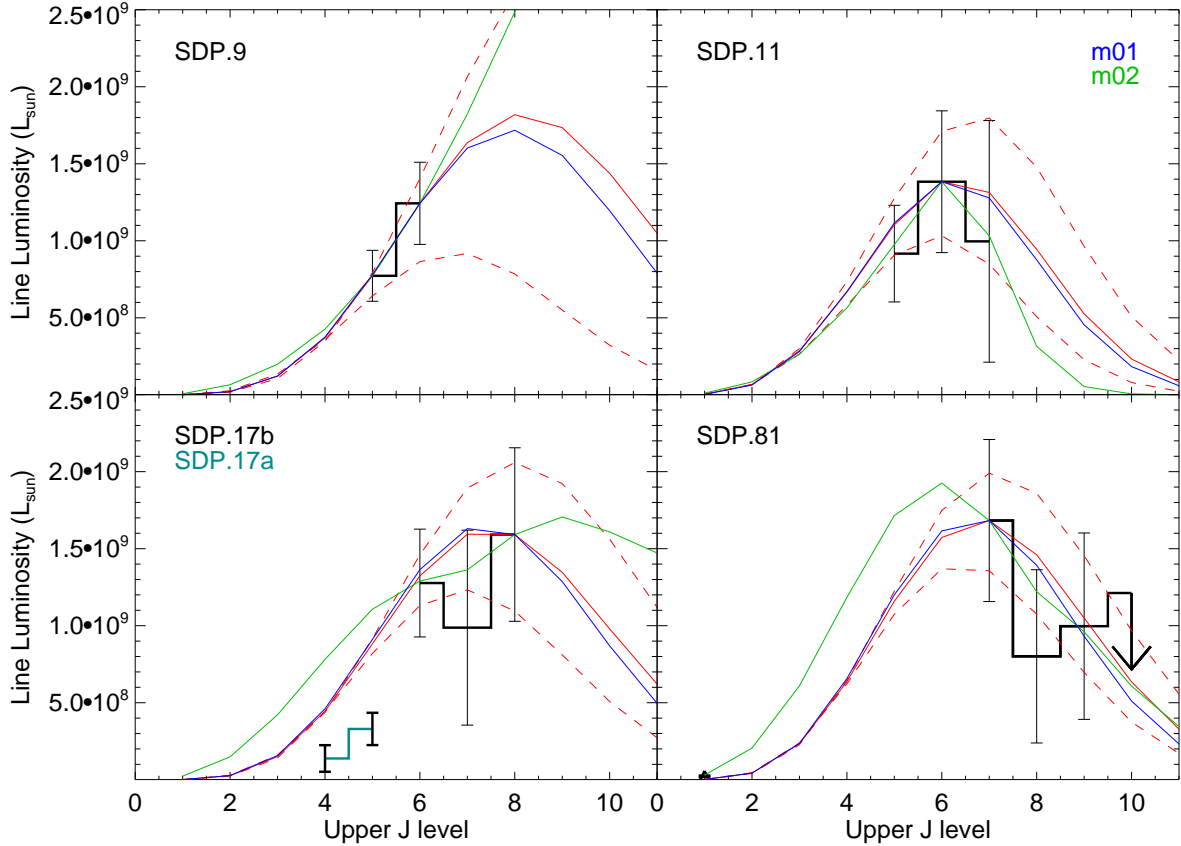


Fig. 9.— Spectral line energy distributions, uncorrected for gravitational lensing magnification. The Z-Spec measurements are shown connected by the black histogram. The data point for the CO(1-0) line measured by Frayer et al. (2010) in SDP.81 falls at the bottom of the panel, and is better seen in Figure 12. The red lines show the SLEDs predicted by the best-fit LTE model (continuous), and the LTE models corresponding to the limits of the 1σ standard confidence interval for T_{ex} determined from the fit (dashed). The blue line corresponds to the SLED predicted by RADEX using the same temperature and column density as the LTE model, while the green line shows the SLED predicted by RADEX with the parameters given by the 4D maximum likelihood solution. The parameters for these two RADEX models, m01 and m02, respectively, are listed in Table 5.

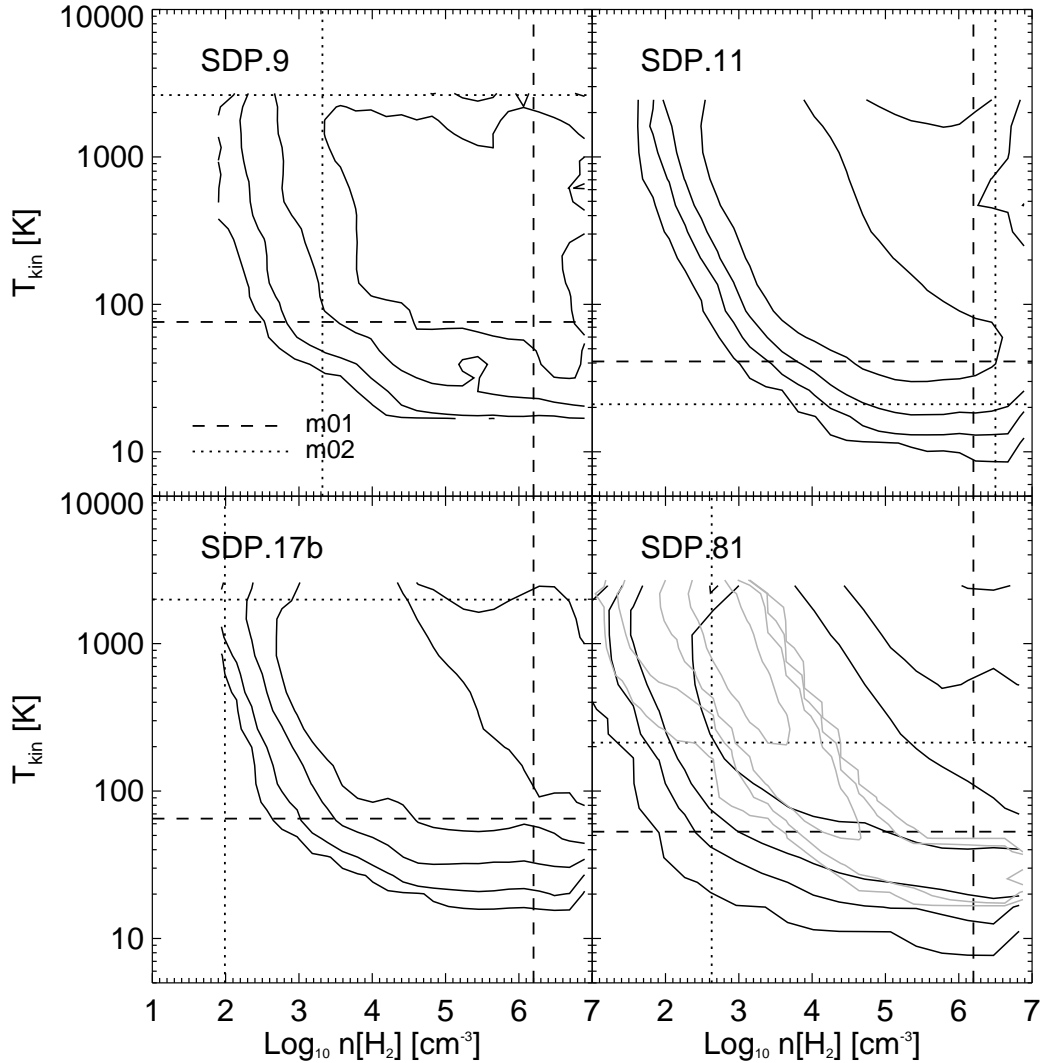


Fig. 10.— Contour plots of the $(T_{kin}, n[\text{H}_2])$ 2D marginal likelihood distributions, generated by a MCMC sampling of the parameter space for RADEX models. The contours are in $n\sigma$ -equivalent steps, enclosing 68.3%, 95.4%, 99.7%, and 99.99% of the probability, respectively. The dashed lines correspond to parameters that reproduce the LTE solution (model m01), and the dotted lines indicate the parameters corresponding to the RADEX 4D maximum likelihood solution (model m02). Note that the 2D marginal distributions will not necessarily have the same maximum as the 4D distribution. The kinetic temperature is limited to 3000 K, where collisional dissociation of CO becomes important. In the SDP.81 panel, the lighter contours show the probability levels for a model including the CO(1-0) from Frayer et al. (2010). The parameters for this model are listed as model m03 in Table 5.

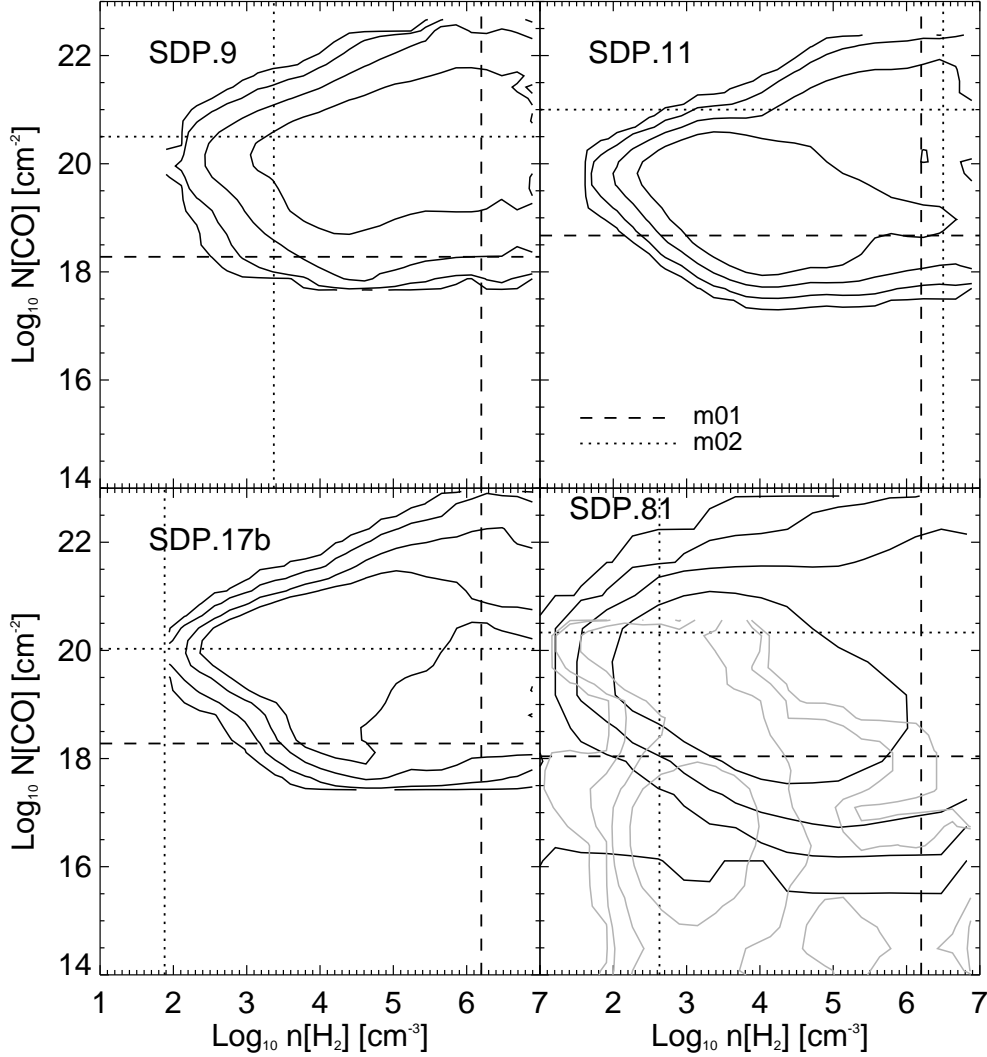


Fig. 11.— Same as Figure 10 for the $(N[\text{CO}], n[\text{H}_2])$ 2D marginal likelihood distributions.

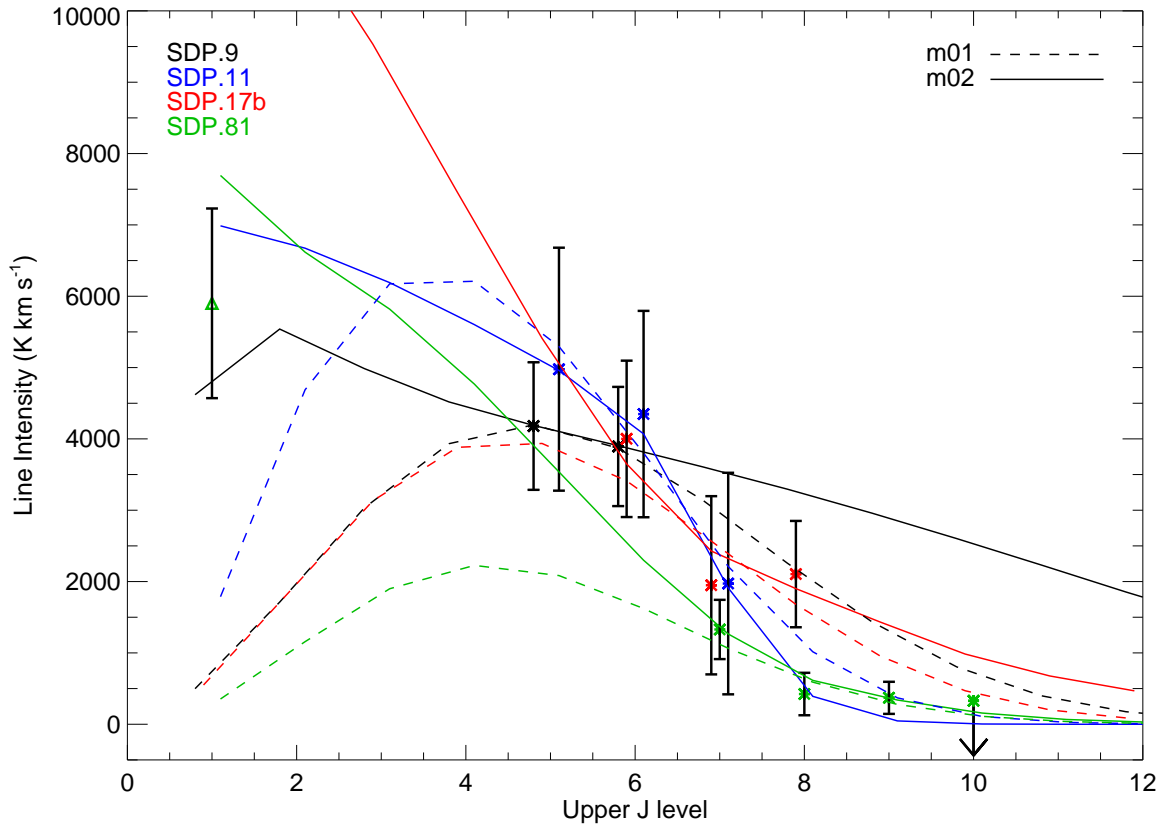


Fig. 12.— $W(J)$ as a function of transition for four of the galaxies in our sample. For clarity, the values for the same transition in different galaxies have been slightly offset around the position of the upper J level. The triangle point represents the intensity of the CO(1-0) line for SDP.81 measured by Frayer et al. (2010). The $W(J)$ distributions predicted by the RADEX models m01 and m02 are shown with a dashed and continuous line, respectively. These lines emphasize the constraints on the allowed parameter space that can be gained by having measurements of both higher and lower J transitions.